AN ABSTRACT OF THE THESIS OF

Kevin J. Drost for the degree of Master of Science in Mechanical Engineering and Environmental Geology presented on June 4, 2012.

Title: RANS and LES Predictions of Turbulent Scalar Transport in Dead Zones of Natural Streams

Abstract approved: _____

Sourabh V. Apte   Roy Haggerty

Natural stream systems contain a variety of flow geometries which contain flow separation, turbulent shear layers, and recirculation zones. This work focuses on streams with dead zones. Characterized by slower flow and recirculation, dead zones are naturally occurring cutouts in stream banks. These dead zones play an important role in stream nutrient retention and solute transport. Previous experimental work has focused on idealized dead zone geometries studied in laboratory flumes. This work explores the capabilities of computational fluid dynamics (CFD) to investigate the scaling relationships between flow parameters of idealized geometries and the time scales of transport. The stream geometry can be split into two main regions, the main stream flow and the dead zone. Geometric parameters of the dead zone as well as the bulk stream velocity were varied to determine a scaling relationship for the transport time scales. These flow geometries are simulated

using the RANS turbulence model with the standard k-ω closure. The standard first order dead zone model is expanded to a two region model to accommodate the multiple time scales observed in the simulation results. While this model currently has limited predictive capability, it provides physical insight into the functional dependence of the dead zone time scales. LES is used to evaluate the performance of the Reynolds Averaged Navier-Stokes (RANS) turbulence model and to describe the anisotropic turbulence characteristics. The differences between the time averaged flow field for Large Eddy Simulation (LES) and RANS was determined to have a significant impact on passive scalar transport.

RANS and LES Predictions of Turbulent Scalar Transport in Dead
Zones of Natural Streams

by

Kevin J. Drost

A THESIS

submitted to

Oregon State University

in partial fulfillment of
the requirements for the
degree of

Master of Science

Presented June 4, 2012
Commencement June 2012

Master of Science thesis of Kevin J. Drost presented on June 4, 2012.

APPROVED:

_____

Co-Major Professor, representing Mechanical Engineering

_____

Co-Major Professor, representing Environmental Geology

_____

Head of the School of Mechanical, Industrial, and Manufacturing Engineering

_____

Dean of the Graduate School

I understand that my thesis will become part of the permanent collection of Oregon State University libraries. My signature below authorizes release of my thesis to any reader upon request.

_____

Kevin J. Drost, Author

ACKNOWLEDGEMENTS

TABLE OF CONTENTS

TABLE OF CONTENTS (Continued)

LIST OF FIGURES

LIST OF TABLES

LIST OF APPENDICES

LIST OF APPENDIX FIGURES

LIST OF APPENDIX TABLES

RANS and LES Predictions of Turbulent Scalar Transport in Dead Zones of Natural Streams

Chapter 1: Introduction

The properties of dead zones are important for many engineering as well as hydrologic applications. A dead zone is a region within a flow characterized by slower moving fluid and reduced mixing. Reduced mixing can make the dead zone a region of significantly different properties compared to the average flow. In general, dead zones are caused by changes in the geometry of the boundaries. This work will focus on dead zones in open channel flows. The channel flow can be described by an average velocity, depth, and span. A free surface also exists between the channel fluid and the surrounding fluid, typically air. The channel fluid will depend on application.

Dead zones have been widely studied in engineering applications. Chemical engineers have studied dead zones as they occur in chemical reactors. If a dead zone exists in a reactor, the reduced mixing leads to a reduced reaction rate and thus reduced performance. Generally, reactors are designed to avoid dead zones. When a dead zone is unavoidable, it is important to predict its effect on the reactor. Dead zones are also important in heat transfer applications. The reduced mixing and fluid velocity in a dead zone can lead to a hot spot within the system. A hot spot would lead to a less uniform temperature distribution at the exit and could also damage the material of the channel wall.

This work will focus on dead zones in open channel water flows. These channel

flows have smooth regular boundaries and are an approximation of natural streams. In streams, dead zones are formed by changes in the shape of the bank. These dead zones play an important role in a stream's response to changes in dissolved substances. These substances could be dissolved nutrients or pollutants. Nutrients will effect the aquatic habitat within the dead zone. A release of dissolved nutrients will quickly be advected downstream. The reduced mixing will cause the dead zone to remain nutrient rich over a longer period of time thus allowing aquatic plants and animals more time process the nutrients. For the same reason, the concentration of a release pollutant will remain higher in a dead zone. The characteristics of the dead zone will determine how long the stream stays at a toxic levels and where cleanup workers should focus their work.

A channel with a dead zone can be simplified down to group of important parameters. Figure 1.1 shows a rectangular dead zone with the important dimensions labeled. The length, L, is measured in the streamwise direction; width, W, in the spanwise direction; and depth, D, in the vertical direction. The velocity scale, U, is defined as the average channel velocity. A Reynolds number can be defined based on the depth, velocity, and viscosity and is shown in Equation 1.1.

$$Re_D = \frac{DU}{\nu} \tag{1.1}$$

Two additional depths can be specified for when the dead zone and main channel have different depths, the depth at the exchange boundary between the main channel and the dead zone, h_E, and the average dead zone depth, h_D. These dimensions

are straightforward to measure for a rectangular dead zone. Average lengths and widths could be determined for irregularly shaped dead zones. Figure 1.2 shows an example of a naturally occurring dead zone in a stream.
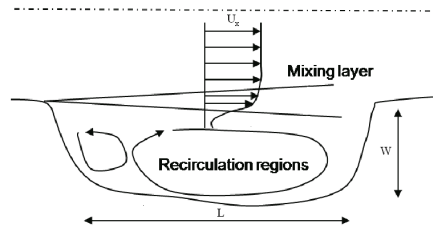
Figure 1.1: Schematic of a typical dead zone showing the mixing layer and streamwise velocity profile. W is measured in the spanwise direction. L is measured in the streamwise direction.

Figure 1.2: A natural dead zone caused by an obstruction in a stream. The main channel flow is from right to left.

In streams, dead zones can be caused by obstructions in the main channel flow or lateral cavities in the bank. In both cases, a sudden change in bank geometry causes the main channel flow to separate from bank. A shear layer forms between the fast moving main channel flow and the slower moving dead zone flow. Diffusion of momentum across the shear layer drives recirculating flow inside the dead zone.

This recirculating flow can take many forms depending on the dead zone shape and main channel velocity. All dead zones have at least one eddy that is formed by the recirculation. Understanding the fluid properties of the shear layer and recirculation is critical to understanding the properties of the dead zone as a whole.

Current methods for characterizing the properties of dead zones involve measuring the residence time of a dissolved chemical tracer. The tracer is nontoxic but can be detected using sensors within the dead zone. The chemical is injected into either the stream or the dead zone. The concentration in the dead zone changes over time and the response indicates the residence time. While this type of experiment has been used extensively, it has limitations. The measured residence time depends somewhat on the location of the sensors in the dead zone. These tests can also take a considerable amount of time to complete. In order to get the stream response to a sudden change in a dissolved chemical, a tracer test would need to be run for each dead zone along the length of stream of interest.

The goal of this work is to understand the important fluid quantities that affect the residence time of a dead zone. Using these fluid quantities and a simplified model of the dead zone, the residence time could be predicted based on the basic dimensions of the dead zone and stream. If such a prediction were sufficiently accurate, it would greatly reduce the time required to get the residence time of a length of stream. This work uses computational fluid dynamics (CFD) to simulate a stream/dead zone system with the goal of determining what dimensions affect the residence time. Both Reynolds Averaged Navier-Stokes (RANS) and Large Eddy Simulation (LES) turbulence models are used.

Chapter 2: Literature Review

2.1   Dead Zones

Early work on quantifying the transport properties of dead zones focused on developing a simplified model for the interaction between the dead zone and the main channel. Valentine and Wood [43] conducted laboratory experiments on simplified dead zones. These experiments found that the exchange process can be modeled as a first order system by assuming the dead zone to be perfectly mixed (see the Dead Zone Models section for more details). Valentine and Wood [42] found that the exchange coefficient was approximately constant for a variety of dead zone geometries. This first order dead zone model was then combined with the axial dispersion model used by Levenspiel [21] to model the response of the combination of stream and dead zone. A good review of residence time theory with applications in engineering and hydrology is provided by Nauman [32].

Bencala and Walters [4] did experiments in natural streams and compared the results to the axial dispersion model and found adequate agreement. However, they recognized the need to predict the model parameters instead of fitting the model to existing results. Leibundgut et al. [20] continued this work by applying the advection diffusion model to tracer experiments in the Rhine river. The results were found to accurately model pollutant transport for this river.

Engelhardt et al. [8] later conducted large scale experiments on irregularly shaped dead zones in the River Elbe. These experiments showed that the exchange process relies on coherent eddies shed from the upstream corner of the dead zone. As these eddies travel downstream through the mixing layer, their influence penetrates into the dead zone. These structures are quasi-two dimensional. Kimura and Hosada [15] compared laboratory experiments to numerical results using the depth-averaged equations. The depth-averaged equations captured the same average velocity trends as the experiments with the largest differences in the mixing layer.

Engelhardt also found that the exchange process for the irregular dead zones had many time scales and thus could not be represented as a first order system. Additional experiments on the River Elbe by Kozerski et al. [16] showed that the exchange process is complicated by a dead zone having regions of distinctly different flow characteristics. In this case, the dead zone can be modeled as a combination of sub regions. Each sub region is modeled as a first order system.

Recently Uijttewaal et al. [41] conducted laboratory flume studies on series of dead zones. A series of dead zones is less likely to appear naturally in streams, but can be found where human made structures have been introduced to control erosion or to help habitat restoration. These experiments varied geometric and flow parameters. The exchange coefficient was generally insensitive to changes in geometry and the flow. Dye concentration studies show that the system can be approximated as a first order system. However, the system is more complicated as the exchange coefficient changes over time. Particle tracking results show a

primary eddy located near the center of the dead zone with a secondary eddy in the upstream corner of the dead zone. The existence of the secondary eddy is hypothesized to contribute an additional time scale to the exchange process.

Weitbrecht [46] also conducted tracer experiments on a series of dead zones in a laboratory flume. These experiments focused on parametric studies for many different geometric features. Weitbrecht found that the aspect ratio, defined as $\frac{W}{L}$ of the dead zone determines how many eddies will be present. For aspect ratios around unity, only one eddy is present. As the aspect ratio is increased or decreased, secondary eddies are formed. Using a combination of dye concentration and particle tracking studies, Weitbrecht found that the exchange coefficients generally matched the results of Valentine and Wood [42], and Uijttewaal [41]. However, the coefficient varied slightly based on the geometry of the dead zone. Weitbrecht proposed using a modified hydraulic diameter to combine geometric terms into a shape factor.

Bellucci et al. [3] conducted an analytical investigation of the advection-diffusion equation for semi-enclosed basins assuming a constant eddy diffusivity. The residence times of these basins could be characterized by multiple time scales. Using an analysis of eigenvalues Bellucci showed that the average concentration of a passive scalar will always become exponential given enough time. These results are applicable to flows with recirculation like dead zones.

Recent experimental studies have taken advantage of full field velocity measurement techniques such as particle tracking velocimetry (PTV) [41, 46, 49, 17] and particle image velocimetry (PIV) [34, 24] to capture higher resolution and

transient behavior of dead zones. PTV is generally conducted with floating particles and therefore only measures velocities at the free surface. These types of studies have all found similar flow structures within dead zones with a variety of geometries. There is generally a primary eddy that exchanges momentum with the main channel through a shear layer. Lin and Rockwell [24] did extensive work to characterize the turbulence properties in the shear layer near a rectangular cavity.

2.2 Numerical Techniques

Numerical simulations have been used extensively to model flows in natural systems. Yao et al. [48] have done simulations of cavity type dead zones in laminar flows. Despite being laminar, these flows showed a primary eddy and shear layer similar to turbulent flume studies. For turbulent flows, RANS-based simulations have an extensive history in applications to natural flows.

Biglari and Sturm [5] have done depth-averaged k-ϵ based RANS studies of flow around a bridge abutment protruding into a channel. This work found that the RANS model predicted the mean flow reasonably well around the abutment. Ouillon and Dartus [33] also used RANS to look at an obstruction in channel flow. Their three dimensional simulations found good agreement between the simulations and experiments for the flow reattachment location.

Geometries with cavities have also been explored with RANS models. Gualtieri et al. [11] did RANS simulations of flow past a two dimensional rectangular cavity and found that the Reynolds Stress model matched experiments better than the

k-ϵ model. Tritthart et al. [40] did RANS studies of a series of dead zones in a natural river and used a random walk scheme to model the transport of dissolved substances. Many studies have used a RANS-based passive scalar analysis to model the transport of pollutants or nutrients for a variety of geometries [35, 39, 36, 2, 11].

In engineering application, LES has been used extensively due to its increased accuracy and predictive capability compared to RANS models. For natural systems, LES has been successfully applied to channel flows. Van Balen et al. [44] showed that LES predicts mean velocities accurately as well as higher order statistics. For high speed flow, LES studies by Shams [37] have been shown to give good agreement with experiments by Lui and Katz [25] for flows over a cavity. LES studies show similar flow patterns to RANS studies [6].

LES has also been applied to scalar transport problems within dead zones. McCoy et al. [28, 29] did extensive studies of flow past an obstruction-type dead zone. These studies showed that the scalar concentration had at least two time scales and that the scalar exchange is not uniform in the vertical direction. Hinterberger [13] also showed a depth dependence by comparing full three dimensional LES with a depth-averaged formulation for a series of obstruction-type dead zones. These results highlight the need for fully three dimensional studies when analyzing open channel flows past dead zones.

McCoy et al. [30] and Constantinescu et al. [7] did three dimensional LES of a series of dead zones matching the geometry used in experiments by Uijttewaal [41]. These studies showed that LES matches the experiments better than the corresponding RANS simulations. Constantinescu completed a passive scalar study

using LES and found that the exchange coefficient is in the same range as experimental results. Another study by Larcheveque [19] also found LES to provide better predictions for flow over a cavity when compared to RANS and detached eddy simulations.

Chapter 3: Mathematical Formulation

This section will describe the governing equations, assumptions, and models used in the study of open channel flow with a lateral dead zone. The first step is to do a dimensional analysis of the problem to determine what physical quantities and nondimensional groups are important.

3.1   Dimensional Analysis

There are many important physical quantities to a natural dead zone including bed roughness and many geometric quantities to describe the irregular shape of the bank. This analysis is restricted to smooth geometries with rectangular lateral cavities. The bed surface is allowed to have a constant slope as shown in Figure 3.1.

The parameter of interest is the exchange velocity between the dead zone and the main channel. Dimensional analysis begins with a list of the dimensional variables that affect the variable of interest. In this case $E = f(U, \nu, L, W, D, h_E, h_D, S, g)$ where E is the exchange velocity, U is the average channel velocity, ν is the kinematic viscosity of the fluid, L is the dead zone length in the streamwise direction, W is the dead zone width in the spanwise direction, D is the main channel depth, h_E is the depth at the exchange between the dead zone and the main channel, h_D
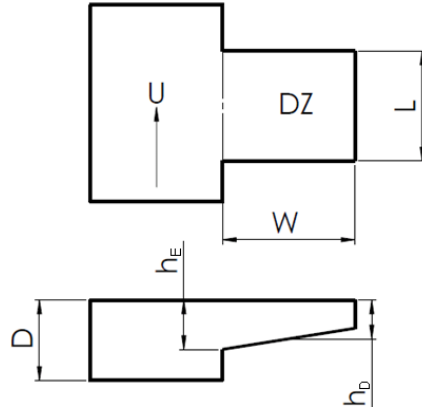
Figure 3.1: Plan view and cross section of a simplified dead zone with the standard dimensions labeled.

is the average depth of the dead zone, S is the span of the main channel, and g is the gravitational constant. Compressibility effects are neglected due to the low velocities considered and the high acoustic velocity of water.

The span is assumed to be large compared to the size of the dead zone shear layer and thus have a negligible impact on exchange. The remaining variables can be arranged in nondimensinonal groups. These groups are not unique as other nondimensional groups can be formed by combining two or more of these groups. The result is shown in Equation 3.1 where Re_W is the Reynolds number based on the width and Fr_D is the Froude number based on the depth shown in Equation 3.2.

$$\frac{E}{U} = f(Re_W, \frac{W}{L}, \frac{W}{D}, \frac{h_E}{D}, \frac{h_D}{D}, Fr_D) \tag{3.1}$$

$$Fr_D = \frac{U}{\sqrt{gD}} \tag{3.2}$$

The Froude number is a ratio of the average velocity in the channel to the

velocity of shallow water waves at the free surface. Thus this nondimensional number is a measure of the importance of free surface effects. For all the cases studied in this work, the Froude number is below 0.4. Therefore, it is a reasonable assumption to neglect free surface effects all together. This is implemented by removing the gravity force term and replacing the free surface with a rigid flat lid. This leaves the exchange velocity as a function of a Reynolds number and four geometric ratios.

3.2   Governing Equations

The governing equations for fluid flow and scalar transport come from conservation relationships. The fluids problem is governed by conservation of fluid mass and momentum. This work uses two assumptions to simplify the problem. First, the fluid density is constant as compressibility effects are neglected and the flow is considered isothermal. Secondly, the viscosity is constant as the flow is isothermal and water can be assumed to be Newtonian. With these assumptions the continuity and Navier-Stokes equations, the conservation of mass and momentum respectively, are shown in Equations 3.3 and 3.4.

$$\frac{\partial u_i}{\partial x_i} = 0 \tag{3.3}$$

$$\frac{\partial u_i}{\partial t} + u_j \frac{\partial u_i}{\partial x_j} = -\frac{1}{\rho}\frac{\partial P}{\partial x_i} + \nu \frac{\partial^2 u_i}{\partial x_j \partial x_j} \tag{3.4}$$

These equations fully describe the transient, three dimensional velocity and pressure field. In order to simulate the injection of a tracer, a passive scalar transport equation can be written to conserve the mass of the tracer. Equation 3.5 is the transient advection diffusion equation for a passive scalar. The Schmidt number (Sc) is defined in Equation 3.6 where D_m is the molecular diffusion of a particular dissolved substance in water.

$$\frac{\partial C}{\partial t} + u_j \frac{\partial C}{\partial x_j} = \frac{1}{Sc} \nu \frac{\partial^2 C}{\partial x_j \partial x_j} \tag{3.5}$$

$$Sc = \frac{\nu}{D_m} \tag{3.6}$$

Equations 3.3, 3.4, and 3.5 are a coupled system of nonlinear partial differential equations. While these equations can be solved numerically directly, the computational cost makes it impractical for many turbulent flows. All of the cases in this work are turbulent as the $Re_D > 2000$. A turbulent flow has a wide range of length and time scales. A direct solution requires resolution of the smallest scales greatly increasing the computational cost. Another option is to model some of the scales and thus reduce the cost of the problem. This work uses two different modeling approaches to model part of the turbulence.

3.3   RANS Turbulence Model

A useful technique in reducing the size of a fluids problem is called Reynolds Averaging. When applied to the Navier-Stokes equation, 3.4, this is called the

Reynolds Averaged Navier-Stokes (RANS). Reynolds Averaging takes each variable and divides them into mean and fluctuating components. Equations 3.7 and 3.8 shows the standard notation with an over bar signifying a time averaged quantity and a prime signifying a fluctuating quantity. Equations 3.7 and 3.8 can be substituted into the continuity and Navier-Stokes equations. Next, each equation is time averaged. Using the rules of averaging, these equations can be simplified down to Equations 3.9 and 3.10.

$$u_i = \overline{u}_i + u' \tag{3.7}$$

$$P = \overline{P} + P' \tag{3.8}$$

$$\frac{\partial \overline{u}_i}{\partial x_i} = 0 \tag{3.9}$$

$$\overline{u}_j \frac{\partial \overline{u}_i}{\partial x_j} = -\frac{1}{\rho}\frac{\partial \overline{P}}{\partial x_i} + \frac{\partial}{\partial x_j}\left(\nu \frac{\overline{u}_i}{\partial x_j} - \overline{u'_i u'_j} \right) \tag{3.10}$$

Equations 3.9 and 3.10 form a system of coupled partial differential equations and can be solved for the mean pressure and velocity fields if the $\overline{u'_i u'_j}$ term is known. In general, this term is not known and must be modeled in order to close the system of equations. $\rho \overline{u'_i u'_j}$ is called the Reynolds Stress Tensor. While this term is actually derived from the nonlinear advective terms in the Navier-Stokes Equation, by convention it is moved to the right hand side and grouped with the viscous stress term. The Reynolds Stresses can be conceptualized as the additional stresses caused by turbulent fluctuations. This work uses the gradient diffusion hypothesis to model the Reynolds Stresses as a diffusion-like process that

is proportional to the mean stress tensor. For an incompressible fluid, this model simplifies down to Equation 3.11 where ν_T is the eddy viscosity. Using ν_T in Equation 3.10 gives Equation 3.12.

$$\overline{u_i' u_j'} = -\nu_T \frac{\partial \overline{u}_i}{\partial x_j} \tag{3.11}$$

$$\overline{u}_j \frac{\partial \overline{u}_i}{\partial x_j} = -\frac{1}{\rho} \frac{\partial \overline{P}}{\partial x_i} + (\nu + \nu_T) \frac{\partial^2 \overline{u}_i}{\partial x_j \partial x_j} \tag{3.12}$$

Now only the eddy viscosity needs to be calculated to close the problem. There are a variety of methods for calculating the eddy viscosity. Generally, there is a tradeoff between computational expense and accuracy. This work uses the k-ω two-equation model. This model introduces two additional transport equations for k, the turbulent kinetic energy (TKE), and ω, the specific dissipation rate. The TKE is defined as $\frac{1}{2}\overline{u_i' u_i'}$. The specific dissipation rate is the rate at which TKE is dissipated per unit TKE. The resulting transport equations for k and ω have many nonlinear terms. Wilcox originally derived these transport equations and a detailed description can found in his 1988 paper [47]. The two equations require five model constants to be closed. These constants are found empirically for a given flow geometry reducing the generality of this model. The complete transport equations for k and ω are in Appendix A along with the model constants used and a brief explanation of why this model was selected. The eddy viscosity is calculated as a ratio of k and ω as shown in Equation 3.13. Knowing the eddy viscosity fully closes the model and time averaged values can be calculated for pressure, velocities,

TKE, and specific dissipation rate.

$$\nu_T = \frac{k}{\omega} \tag{3.13}$$

A similar procedure can be done for the scalar transport equation where the $\overline{C'u_j'}$ term is closed with the gradient diffusion hypothesis resulting in Equation 3.14. The turbulent Schmidt number is introduced as the ratio of the turbulent viscosity to the turbulent scalar diffusivity, Equation 3.15 where D_T is the turbulent diffusivity for the scalar. The value of Sc_T is determined empirically. Tominaga and Stathopoulos [39] looked at the optimum Sc_T for different flow configurations and found a range from 0.2-1.2. Rossi and Iaccarino [35] studied scalar transport around the wake of a square obstruction and used a Sc_T value of 0.85. For this work, a value of 0.9 was selected as it has been used by Baik et al. [2] and Santiago et al. [36] for separated flows around blunt objects. Gualtieri et al [11] used a value of 0.9 for flow past a two dimensional rectangular dead zone. The Sc number is assumed to be one. This value would generally depend on the dissolved chemical being modeled. However, for a turbulent flow, the turbulent diffusivity will be at least an order of magnitude larger than the molecular diffusivity.

$$\frac{\partial \overline{C}}{\partial t} + \overline{u}_j \frac{\partial \overline{C}}{\partial x_j} = \left(\frac{1}{Sc}\nu + \frac{1}{Sc_T}\nu_T \right) \frac{\partial^2 \overline{C}}{\partial x_j \partial x_j} \tag{3.14}$$

$$Sc_T = \frac{\nu_T}{D_T} \tag{3.15}$$

RANS simulations have the benefit of requiring coarser grids and thus are com-

putationally cheaper. This comes at the cost of reduced information about the flow, as all variables are time averaged, including the turbulence quantities. RANS closure models have been successfully used for a variety of flows. However, the model constants must be tuned using experimental results or more detailed simulations. This disadvantage limits the predictive capability of RANS simulations.

3.4 LES Turbulence Model

While RANS models significantly reduce the computational cost of a given flow system, the time averaging removes the transient information. This information can play an important role in turbulent flows. Large eddy simulations (LES) are a compromise between RANS and solving the Navier-Stokes equations directly.

Turbulent flows contain many different scales. The largest or integral scale is based on the largest physical dimension in the system. For a dead zone, the integral length scale would be a measure of the dead zone size. The smallest length scale is the Kolmolgorov length scale. At this small size, viscous effects dominate inertia and damp out fluctuations. The Kolmolgorov length scale describes where the turbulent energy is dissipated in the system. This idea leads to the study of how energy is transferred to the Kolmolgorov length scale.

Analyzing the energy content of a turbulent flow has led to the idea of an energy cascade shown in Figure 3.2. This conceptualization tracks the turbulent energy of the flow from generation to dissipation. Turbulent energy is generated at the integral length scale where the fluctuations are largest but have the smallest

wave number. Eddies at this scale are unstable and break down into smaller and smaller eddies until the Kolmolgorov length scale where the energy is dissipated. In between the integral and Kolmolgorov scales are all of the eddies that are neither generating or dissipating energy. These eddies only transfer energy to smaller scales. These categories are given the following names: the energy containing range where majority of the TKE is generated and held, the inertial sub range where energy is transferred to smaller scales, and the dissipative range where energy is dissipated by molecular viscosity.
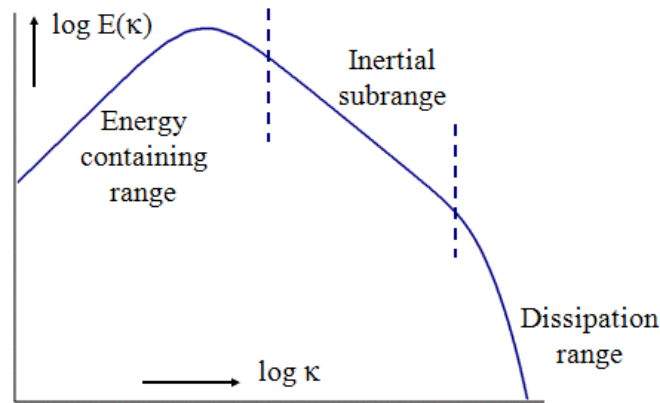
Figure 3.2: Conceptualization of the energy cascade of the turbulent energy content of a flow as a function of the wavenumber.

LES takes advantage of the difference between these scales to resolve only the scales that contain a significant amount of energy. The other scales are modeled. This requires a spatial filter. All eddies larger than the filter size are resolved. The smaller eddies along with their corresponding small time scales are removed and need to be modeled. In a simulation, the grid size is generally used as a convenient filter size. The goal is to have the smallest resolved scales in the inertial sub range.

This saves the computational cost that would be spent resolving the smallest scales and still resolves the largest scales that have the most significant impact on integral scale parameters.

The derivation of the LES equations begins by filtering the continuity and complete Navier-Stokes equations, Equations 3.3 and 3.4. Applying the filtering rules, gives Equations 3.16 and 3.17 where aˆ term is a grid filtered variable. The effect of the small scales is contained in the subgrid-scale (SGS) stress term defined in Equation 3.20. This term must be modeled to close the set of equations.

$$\frac{\partial \hat{u}_i}{\partial x_i} = 0 \tag{3.16}$$

$$\frac{\partial \hat{u}_i}{\partial t} + \hat{u}_j \frac{\partial \hat{u}_i}{\partial x_j} = -\frac{1}{\rho}\frac{\partial \hat{P}}{\partial x_i} + \nu \frac{\partial^2 \hat{u}_i}{\partial x_j \partial x_j} - \frac{\partial \tau_{ij}}{\partial x_j} \tag{3.17}$$

$$\tau_{ij} = \widehat{u_i u_j} - \hat{u}_i \hat{u}_j \tag{3.18}$$

The Smagorinsky [38] model approximates the SGS stress with the gradient diffusion hypothesis. This assumes that the SGS stress is diffusion-like and proportional to the resolved stress. The SGS viscosity, ν_{SGS} is defined as

$$\nu_{SGS} = \left(C_S \hat{\Delta}\right)^2 |\hat{S}| \tag{3.19}$$

where C_S is the Smagorinksy constant, $\hat{\Delta}$ is the filter size, and $\hat{S}$ is the resolved

strain-rate tensor defined as

$$\hat{S} = \frac{1}{2} \left(\frac{\partial \hat{u}_i}{\partial x_j} + \frac{\partial \hat{u}_j}{\partial x_i} \right) \tag{3.20}$$

and the magnitude of $\hat{S}$ is defined as

$$|\hat{S}| = \sqrt{2 \hat{S} \hat{S}} \tag{3.21}$$

Substituting these definitions into the filtered Navier-Stokes, Equation 3.17 gives Equation 3.22. C_S is typically in the range of 0.1-0.2 and is assumed independent of location and flow conditions. This assumption prevents the model from accurately predicting flows near a wall and in transition to turbulence. Germano et al. [9] proposed a method for dynamically calculating the value of C_S based on local flow variables. This model works on the assumption that the SGS stress behaves similarly to the smallest resolved stress. This approximation allows C_S to be a function of space and time and eliminates the need to select a value for C_S.

$$\frac{\partial \hat{u}_i}{\partial t} + \hat{u}_j \frac{\partial \hat{u}_i}{\partial x_j} = -\frac{1}{\rho} \frac{\partial \hat{P}}{\partial x_i} + (\nu + \nu_{SGS}) \frac{\partial^2 \hat{u}_i}{\partial x_j \partial x_j} \tag{3.22}$$

This model, commonly called the Dynamic Smagorinsky Model, is derived by taking a second test filter at a larger size than the grid filter. The second filter gives an expression for the twice filtered SGS stress shown in Equation 3.23. By test filtering Equation 3.20 and subtracting Equation 3.23, the resolved or Leonard

stress can be derived as shown in Equation 3.24.

$$T_{ij} = \widetilde{\widehat{u_i u_j}} - \tilde{\hat{u}}_i \tilde{\hat{u}}_j \tag{3.23}$$

$$\mathscr{L}_{ij} = T_{ij} - \tilde{\tau}_{ij} = \widetilde{\hat{u}_i \hat{u}_j} - \tilde{\hat{u}}_i \tilde{\hat{u}}_j \tag{3.24}$$

T_{ij} and τ_{ij} are approximated using the Smagorinsky type model as shown in Equations 3.25 and 3.26 respectively. These modeled stresses can be substituted into the Equation 3.24 yielding Equation 3.27 where M_{ij} is defined in Equation 3.28.

$$T_{ij} = -2C_S \tilde{\Delta}^2 |\tilde{\hat{S}}| \tilde{\hat{S}}_{ij} \tag{3.25}$$

$$\tau_{ij} = -2C_S \hat{\Delta}^2 |\hat{S}| \hat{S}_{ij} \tag{3.26}$$

$$\mathscr{L}_{ij} = -2C_S \hat{\Delta}^2 M_{ij} \tag{3.27}$$

$$M_{ij} = \frac{\tilde{\Delta}^2}{\hat{\Delta}^2} |\tilde{\hat{S}}| \tilde{\hat{S}}_{ij} - \widetilde{|\hat{S}| \hat{S}}_{ij} \tag{3.28}$$

Equation 3.27 represents five independent equations with C_S being the only unknown. Such a system is over defined. Germano et al. [9] originally contracted both sides of Equation 3.27 by S_{ij} to get Equation 3.29. In practice, this method satisfies only one of the five equations for C_S and allowed the denominator of Equation 3.29 to become small making C_S large. Germano et al. [9] proposed averaging C_S over any homogeneous directions in the flow to prevent large C_S values from causing instability. While this method works well for channel flows, the method is

unstable for flows with no homogeneous directions to average over.

$$C_S \hat{\Delta}^2 = \frac{1}{2} \frac{\mathscr{L}_{ij} \hat{S}_{ij}}{M_{mn} \hat{S}_{mn}} \tag{3.29}$$

Lilly [23] proposed a modification to the dynamic model. The five equations for C_S are solved in a least squares approach. Solving this minimization problem shows that the appropriate contraction should use M_{ij} instead of S_{ij} giving Equation 3.30. This method reduces the probability of a large C_S value causing instability. However, a local averaging technique is generally required.

$$C_S \hat{\Delta}^2 = \frac{1}{2} \frac{\mathscr{L}_{ij} M_{ij}}{M_{mn} M_{mn}} \tag{3.30}$$

In this work, all LES cases use the Dynamic Smagorinsky Model. The discretization is done in a kinetic energy conserving manner. One of the SGS model's roles is to dissipate energy. If dissipative numerical schemes are used, the effect of the model can be washed out. The exact discretization scheme is derived by Mahesh et al. [26] and has been shown to perform well in simple and complex geometries [31, 1].

Chapter 4: Dead Zone Models

There are two broad types of dead zones that have been studied, those formed by obstructions protruding into the main flow and those formed by cutouts into the bank. Figure 4.1 shows the difference between the two dead zone types for a series arrangement. The obstruction-type dead zone causes the flow to accelerate around the obstruction as the stream width is decreased. The acceleration and subsequent separation lead to a large recirculation region and a complex shear layer. This type is more representative of an erosion control structure placed in a river or a log protruding into a stream. For the cutout type, the shear layer forms roughly parallel to the flow direction and is similar to a free mixing layer. This type is more representative of naturally formed dead zones in streams. Both types of dead zones can be described by the same geometric parameters and average velocity. For the obstruction-type, the average velocity is calculated before an obstruction is reached.
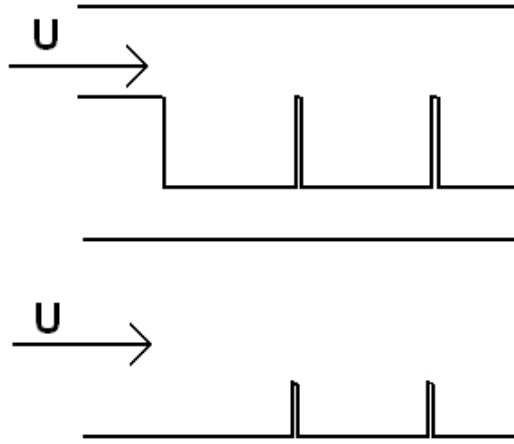
Figure 4.1: A comparison plan views of the two ways dead zones are formed viewed from the top. Top: Dead zone is formed by a cutout into the bank, Bottom: Dead zone is formed by obstructions in the main channel.

4.1 First Order Model

A commonly used model for residence time in a dead zone is the first order model. This model assumes that the dead zone contains a passive scalar at a uniform concentration and that the main channel has a different uniform concentration. Exchange between the main channel and dead zone is specified by a single parameter, the entrainment velocity, E. The uniform concentration in the dead zone is equivalent to a perfectly mixed region, also called a continuously stirred tank reactor (CSTR). Using the entrainment velocity, a non-dimensional exchange coefficient, k, can be formed as a ratio of velocities, Equation 4.1.

$$k = \frac{E}{U} \tag{4.1}$$

Using the definition of k, a mass balance can be written for the mass of the passive scalar in the dead zone, Equation 4.2, where M is the mass of scalar in the dead zone, C is the concentration of scalar in the dead zone, and C_c is the constant scalar concentration of the main channel. Using the definition of k, the definition of concentration as mass per volume, and assuming the concentration of the main channel is zero, the mass balance turns into a first order differential equation, Equation 4.3. Using the initial concentration C_0, the differential equation can be solved for the concentration as a function of time, Equation 4.4.

$$\frac{\mathrm{d}M}{\mathrm{d}t} = -Eh_EL\left(C - C_c\right) \tag{4.2}$$

$$\frac{\mathrm{d}C}{\mathrm{d}t} = -\frac{kUh_E}{Wh_D}C \tag{4.3}$$

$$\frac{C}{C_0} = \exp\left(-\frac{t}{\tau_L}\right) \text{ where } \tau_L = \frac{Wh_D}{kUh_E} \tag{4.4}$$

The first order model is completely defined by the time scale τ_L. For an experimentally obtained normalized concentration curve, fitting an exponential determines the model time scale. Generally, the exponential fit is done for the entire concentration time series. This method gives a single time scale that is a best fit for all the data. Alternatively, the exponential fit can be done as a function of time. This method gives the instantaneous time scale, T, at each data point. Such a series of time scales can be used to assess how well the first order model represents the experimental data. If the time scale changes significantly over time, a more complicated model is needed to capture the dead zone system.

τ_L is the Langmuir time scale and is named after Irving Langmuir who did early analytical work on the mixing of reaction gases [18]. τ_L falls out of the derivation of Equation 4.4 as the total volume of the dead zone divided by the volume flow rate leaving the dead zone. τ_L is a function of physical dead zone measurements, average channel velocity, and the exchange coefficient, k. The physical quantities are straightforward to measure. k has been found to be generally in the range 0.01-0.03 [13, 41, 46, 7, 14]. However, the exact factors that influence the value of k have not been determined.

This first order model has been combined with an axial diffusion model for the main channel to predict the total stream response to a passive scalar [21]. The axial diffusion model assumes the channel has uniform velocity and turbulent diffusion. Such assumptions make the axial diffusion inaccurate when applied to shallow turbulent flows where velocity and turbulent diffusivity have significant gradients.

4.2   Two Region Model

The experimental results of Weitbrecht et al. [46, 45] show that dead zones have a large primary eddy approximately located at the center of the dead zone. The primary eddy separates the dead zone into two regions. There is the core of the primary eddy where the average velocity is small. This region is surrounded by a higher momentum perimeter region. As an extension of the first order model and following the method used by Kozerski et al. [16], the dead zone can be divided into

two perfectly mixed CSTRs. The secondary region concentration, C_s, exchanges scalar with the primary region. The primary region concentration, C_p, exchanges scalar with both the main channel and the secondary region. The addition of a second region increases the number of independent time scales to three as shown in Equation 4.5 where the subscript signifies the two regions that are exchanging scalar. The first subscript is the region who's volume is in the definition.

$$\tau_{pm} = \frac{V_p}{Q_{pm}}, \quad \tau_{ps} = \frac{V_p}{Q_{ps}}, \quad \tau_{sp} = \frac{V_s}{Q_{ps}} \tag{4.5}$$

This formulation does not restrict the secondary region to a particular shape or location. For the two region model to be a significant improvement on the first order model, the primary and secondary regions should have significantly different flow characteristics and thus different time scales. A diagram of one possible combination of primary and secondary regions is shown in Figure 4.2. Using the conservation of mass for a passive scalar, Equations 4.6 and 4.7, two coupled differential equations, can be derived to model the two regions.

$$\frac{dC_p}{dt} = -\frac{C_p}{\tau_{pm}} - \frac{C_p - C_s}{\tau_{ps}} \tag{4.6}$$

$$\frac{dC_s}{dt} = -\frac{C_s - C_p}{\tau_{sp}} \tag{4.7}$$

These two coupled ordinary differential equations can be solved exactly by recasting the equations as a single vector differential equation. The solution is the sum of two exponentials. The time scales of the exponentials are the eigenvalues
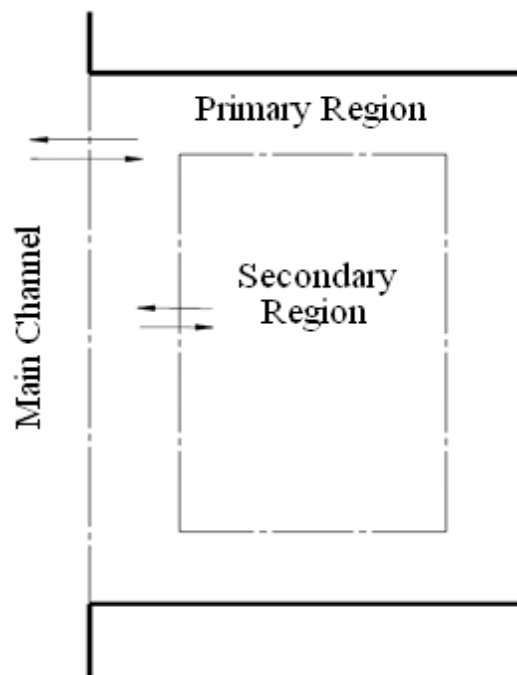
Figure 4.2: Definition of two region geometry. The primary region exchanges directly with the main channel. The secondary region exchanges with the primary region. The precise shape of the secondary region is not specified by the model.

of the coefficient matrix in the vector equation and are given by Equation 4.8. Each eigenvalue corresponds to the time scale of a region. The time scale of the secondary region is assumed to be larger than the primary region time scale. How the exponential terms are weighted is determined by the eigenvectors. The general form of the solution is shown in Equation 4.9 where $\vec{v}$ is an eigenvector.

The constants k_1 and k_2 are determined from the initial conditions of the two regions. The initial conditions depend on the type of tracer study being modeled. Some studies inject the passive scalar into the primary region, wait for the the concentration within the dead zone to reach steady state, stop injection, and then record how the concentration decays in time. To model this type of study, the initial conditions would be found by setting the time derivatives in Equations 4.6 and 4.7 equal to zero. This gives two algebraic equations with the initial conditions as two unknowns. The second commonly used method is to suddenly inject a uniform concentration into the entire dead zone. This gives normalized initial concentration of one for both regions.

$$\tau_p, \, \tau_s = \frac{2}{\frac{1}{\tau_{pm}} + \frac{1}{\tau_{ps}} + \frac{1}{\tau_{sp}} \pm \sqrt{\left(\frac{1}{\tau_{pm}} + \frac{1}{\tau_{ps}} + \frac{1}{\tau_{sp}}\right)^2 - \frac{4}{\tau_{pm}\tau_{sp}}}} \tag{4.8}$$

$$\begin{bmatrix} C_p \\ C_s \end{bmatrix} = k_1 \vec{v}_1 \exp\left(-\frac{t}{\tau_p}\right) + k_2 \vec{v}_2 \exp\left(-\frac{t}{\tau_s}\right) \tag{4.9}$$

The normalized average concentration of the dead zone, C_{DZ}, is the volume weighted average of the two regions as shown in Equation 4.10. This average

can also be written as the sum of two exponentials by substituting Equation 4.9 into the volume weighted average. k_3 is constant that weights the influence of the primary and secondary region time scales. Therefore, two region model has three degrees of freedom, τ_p, τ_s, and k_3. The extra degrees of freedom allow this model to fit more precisely a given concentration time series. This model could be expanded to more than two regions. However, it is important that the fitting parameters retain some physical significance. Ideally, these parameters could be estimated from easily measured geometry and flow quantities.

$$C_{DZ} = \frac{C_s V_s + C_p V_p}{W L h_D} = k_3 \exp\left(-\frac{t}{\tau_p}\right) + (1 - k_3) \exp\left(-\frac{t}{\tau_s}\right) \qquad (4.10)$$

4.3   Model Fitting

Applying either of these models to an experimental or computational concentration plot requires a best fit procedure. The goal is to minimize the error between a given discrete concentration profile and the continuous model profile. In this case, the error is minimized in a least squares sense as shown in Equation 4.11. The first order model fit is straightforward as there is only one parameter to fit. τ_L is fit by taking the best fit slope of a semi-log concentration plot. From Equation 4.4, it can be shown that this slope is the negative and reciprocal of τ_L.

$$E_{fit} = \sqrt{\sum_{i=1}^{n} \left(\frac{|C_i - C_{model}|}{C_i}\right)^2} \qquad (4.11)$$

Fitting the three parameters of the two region model requires an optimization

procedure. This work uses the sequential quadratic programming (SQP) code SNOPT [10]. This code is designed to optimize nonlinear systems with many independent variables and constraints. The procedure works by solving a series of sub problems where the objective function is assumed to be quadratic. The code iteratively finds the location where the gradient of the objective function is zero. For an unconstrained problem, this is equivalent to Newton's method.

The optimization procedure requires initial guesses for the three model parameters. These parameters are put into Equation 4.10 and the model concentration is calculated. Next the fit error is calculated using Equation 4.11. SNOPT then formulates new guesses for the model parameters and the next iteration begins. The iterations continue until a set optimality tolerance is met or a maximum number of iterations is reached.

4.4 Important Time Scales

There are many different time scales that are important to transport within a dead zone. The convective time scale, T_{conv} shown in Equation 4.12, is the time it takes fluid in the main stream to travel the length of the dead zone. This time scale dictates how long an eddy in the mixing layer will affect the dead zone. The Langmuir or volumetric time scale, τ_L in Equation 4.4, is defined as the ratio of the dead zone volume to the volumetric flow rate out of the dead zone. This time scale is the single time scale in the first order model.

Alternatively, a time scale, T, can be fit to a concentration plot as a function

of time according to Equation 4.13. This equation gives a profile of how T changes over time. τ_L is also relevant for the two zone model. From Equation 4.9, it can be shown that the harmonic average of τ_p and τ_s is equal to the harmonic average of τ_{pm}, τ_{ps}, and τ_{sp}. The definitions of T and τ_L, Equations 4.13 and 4.4, imply that τ_L is the minimum possible value of T. T_0 is the time scale the system approaches at late time that is predicted by the analysis of Bellucci et al. [3]. The average residence time, T_{avg} in Equation 4.14, can be found by integrating the normalized concentration curve.

$$T_{conv} = \frac{L}{U} \tag{4.12}$$

$$T(t) = -\left(\frac{d\left(\ln C_{DZ}\right)}{dt}\right)^{-1} \tag{4.13}$$

$$T_{avg} = \int_0^\infty \frac{C}{C_0} dt \tag{4.14}$$

To summarize, for any given dead zone $\tau_L \leq T(t) \leq T_0$ and $\tau_L \leq T_{avg} \leq T_0$. Assuming the first order model implies $\tau_L = T = T_0 = T_{avg}$. Using the two region model, τ_p is assumed to be smaller than τ_s as the primary region interacts directly with the main stream and thus has a larger velocities compared to the secondary region. Using Equation 4.10, τ_L can be shown to be equal to the harmonic mean of τ_p and τ_s weighted by the constant k_3. Therefore the two region model implies that $\tau_L = \left(\frac{k_3}{\tau_p} + \frac{1-k_3}{\tau_s}\right)^{-1} \leq T(t) \leq \tau_s = T_0$.

Chapter 5: RANS Cases

5.1   Solution Procedure

For the RANS simulations, a common solution procedure was adopted to stream-line the process. The first step is to generate a grid. All grids were generated using Pointwise v16.0 [27]. This commercial software is capable of generating structured or unstructured three dimensional grids that can be directly imported into the CFD solver. In Pointwise, surfaces with the same boundary condition are grouped to simplify simulation setup. All RANS simulations are run in Star-CCM+, a commercial finite volume CFD package [12] using the incompressible, isothermal, and turbulent solver options. The turbulence is modeled with the k-ω model using wall functions. Water was chosen as the working fluid with $\rho = 997.6 \frac{\text{kg}}{\text{m}^3}$ and $\mu = 8.89\text{e-}4$ Pa-s.

Before running simulations with dead zone geometries, a fully developed turbu-lent inlet condition needs to be generated. Lien et al. [22] conducted experiments in turbulent channels that could be used to estimate the entrance length. Adding such a long region to each simulation would greatly increase the computational cost of each simulation. For this work, the inlet condition is generated by simulating a simple periodic channel with the same cross section as the eventual inlet surface. The channel needs to have the same boundary conditions for the side walls as the

dead zone geometry. The wall opposite the dead zone is a slip wall to simulate only part of a much wider channel. The top surface is a slip wall to simulate a low Froude number free surface. The bottom and side wall are no-slip boundaries. The channel inlet and outlet are periodic boundaries, meaning all fluid leaving the outlet enters the inlet in order to simulate a long channel. The periodic channel is allowed to evolve until it reaches a steady state solution. The inlet condition is taken from an arbitrary cross section of the channel. For a RANS simulation, the inlet must specify the velocity field and two independent turbulence parameters, turbulence intensity and turbulent viscosity in this case.

With the fully developed inlet information, the dead zone simulation is fully defined. The steady state velocity, TKE, and ω fields are solved for a small section of channel with a dead zone. Next a transient passive scalar analysis is run using Star-CCM+'s implicitly unsteady solver and a one second time step. For this simulation, the flow field is frozen in time and only the passive scalar is allowed to change. The scalar is initialized with a value of one inside the dead zone and zero in the main channel. At each time step, the volume averaged scalar concentration is calculated for the dead zone.

5.2   Series Geometry and Grids

This work contains simulations of two types of dead zone systems, series of dead zones and single dead zones. A series of dead zones can be formed in nature by erosion and deposition processes or by human structures to maintain the depth

of the main channel. These geometries have been studies both experimentally by Weitbrecht [45, 46] and Uijttewaal [41] and numerically by McCoy [30], Constantinescu [7], and Hinterberger [13]. This work studies these series systems as a means of validation and insight into the dynamics of a single dead zone.

Two different series geometries are examined. The first is a cavity type series of dead zones that was studied experimentally by Uijttewaal [41]. Figure 5.1(a) and 5.1(b) show diagrams of this geometry. Each of the six dead zone are 1.125 m long by 0.75 m wide. The dead zone has a linearly sloping bed with an average depth of 0.05 m and a depth of 0.06 m at the main channel dead zone interface. The main channel is 0.1 m deep with an average velocity of 0.35 $\frac{m}{s}$ making $Re_D = 39300$. The x-axis is in the flow direction, y-axis in the vertical direction, and the z-axis in the spanwise direction. This coordinate system is used throughout this work.

Two structured grids, a base and refined, were generated for this geometry. Each grid is most refined in the shear layer between the dead zones and the main channel. The grid coarsens in the spanwise direction away from the dead zone. Diagrams of the grids used are provided in Appendix B. Tables 5.1 and 5.2 have the minimum and maximum grid spacings in both meters and wall units. Wall units are variables scaled by quantities important in the boundary layer near a no-slip wall. Equation 5.1 defines both a friction velocity based on the wall shear stress and a wall length denoted with a plus superscript. The wall shear stress is determined from the mean stress in the periodic channel used to generate the fully
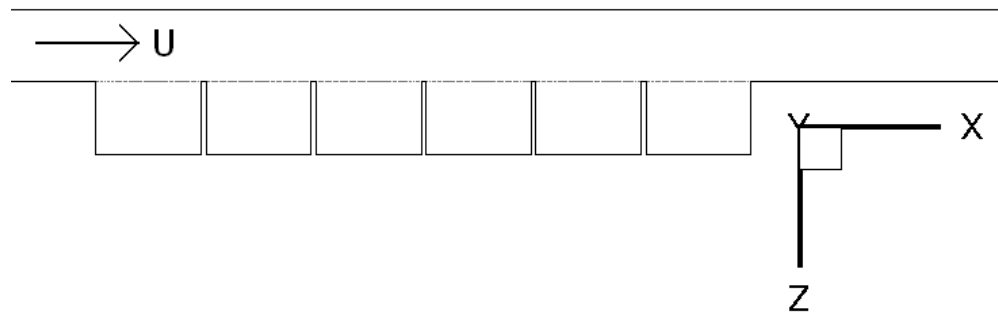
(a) Plan view
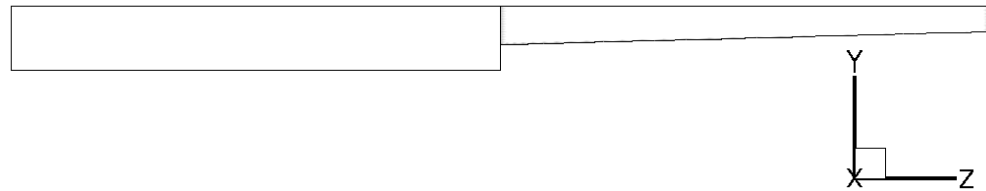
(b) Cross section

Figure 5.1: Description of the geometry for a series of six dead zones matching experiments done by Uijttewaal [41]. Top: Plan view of geometry. Bottom: Cross section of geometry.

developed inlet.

$$y^+ = \frac{yu^+}{\nu}, \text{ where } u^+ = \sqrt{\frac{\tau_w}{\rho}} \tag{5.1}$$

Table 5.1: Base grid sizes, in meters and wall units, used in the shear layer and dead zone for the Uijttewaal geometry. There are different Y spacings for the main channel (MC) and the dead zone (DZ).

	Min [m]	Max [m]		Min	Max
ΔY_{MC}	0.00357	0.004	ΔY_{MC}^+	68.91	77.21
ΔY_{DZ}	0.001	0.0066	ΔY_{DZ}^+	19.30	127.40
ΔX	0.01	0.0335	ΔX^+	193.03	646.64
ΔZ	0.01	0.0366	ΔZ^+	193.03	706.48

Table 5.2: Refined grid sizes, in meters and wall units, used in the shear layer and dead zone for the Uijttewaal geometry. There are different Y spacings for the main channel (MC) and the dead zone (DZ).

	Min [m]	Max [m]		Min	Max
ΔY_{MC}	0.00167	0.00194	ΔY_{MC}^+	32.24	37.45
ΔY_{DZ}	0.000481	0.00658	ΔY_{DZ}^+	9.28	127.01
ΔX	0.005	0.0164	ΔX^+	96.51	316.57
ΔZ	0.01	0.013	ΔZ^+	193.03	250.94

The second series geometry considered matches the experimental design of Weitbrecht [46]. Dead zones in this series are of the obstruction-type that are 1.25 m long, 0.5 m wide, and have a constant depth of 0.046 m in the dead zone and main channel. The average channel velocity is 0.16 $\frac{m}{s}$ making $Re_D = 8260$. Figure 5.2 shows a plan view diagram of this geometry. Organized in Table 5.3 are the minimum and maximum grid spacings. Appendix C contains detailed figures

of the structured grid used.
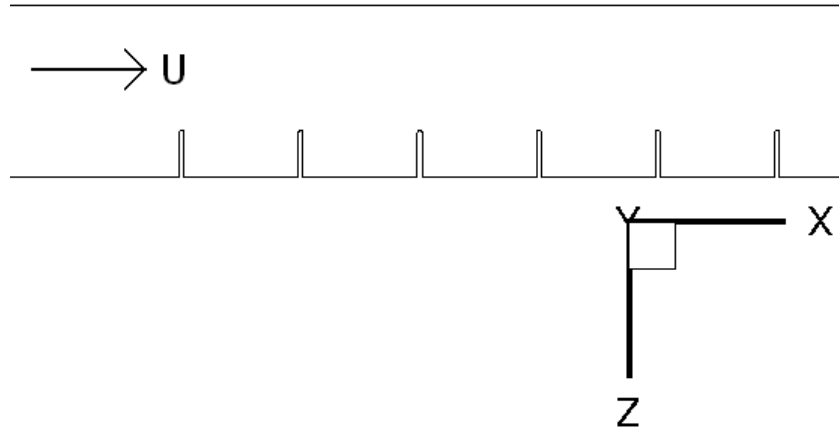
Figure 5.2: Description of the geometry for a series of dead zones matching experiments done by Weitbrecht [46]. This geometry has a uniform depth.

Table 5.3: Base grid sizes, in meters and wall units, used in the shear layer and dead zone for the Weitbrecht geometry.

	Min [m]	Max [m]		Min	Max
ΔY	0.001	0.0068	ΔY^+	11.46	77.94
ΔX	0.01	0.0303	ΔX^+	114.61	347.27
ΔZ	0.01	0.0295	ΔZ^+	114.61	338.10

5.3 Series Validation

In order to validate the chosen grid size, the velocity and TKE results are compared for the base and refined grids for the Uijttewaal geometry. Figure 5.3 shows a velocity profile in the spanwise direction. The velocity decreases traveling from the main channel into the dead zone. The negative velocity in the dead zone is

characteristic of recirculation. The base and refined grids show excellent agreement throughout the dead zone. The refined grid predicts a slightly smaller mixing layer width. Figure 5.4 is a TKE profile in the spanwise direction. As expected, the largest TKE values are at the main channel-dead zone interface where the shear stress generates turbulence. The base and refined grids show good agreement. The refined grid predicts a slightly higher maximum TKE. The velocity and TKE profiles presented are a good representation of profiles taken at other locations in the flow field. The small difference between grids suggest that the refined grid is likely converged. The grid sizes for the other RANS simulations are approximately the same size as this refined grid.
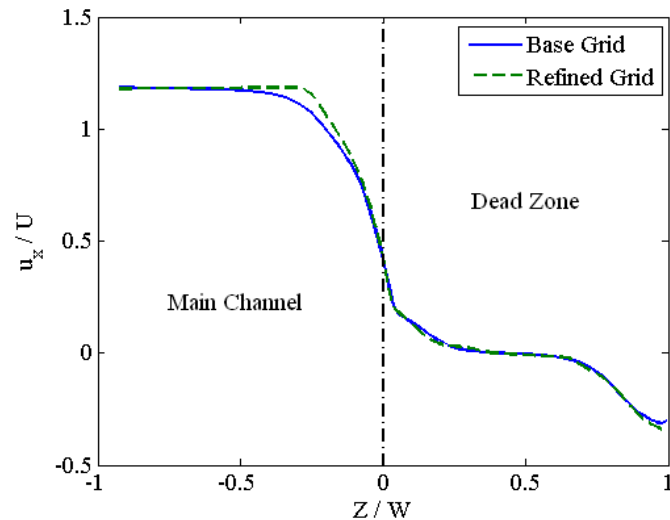
Figure 5.3: Streamwise velocity profile in the spanwise direction for the base and refined grids. Velocity is taken at the free surface and on the centerline of the 5th dead zone in the series using the Uijttewaal geometry.

In order to validate the RANS solver, these simulations are compared to the
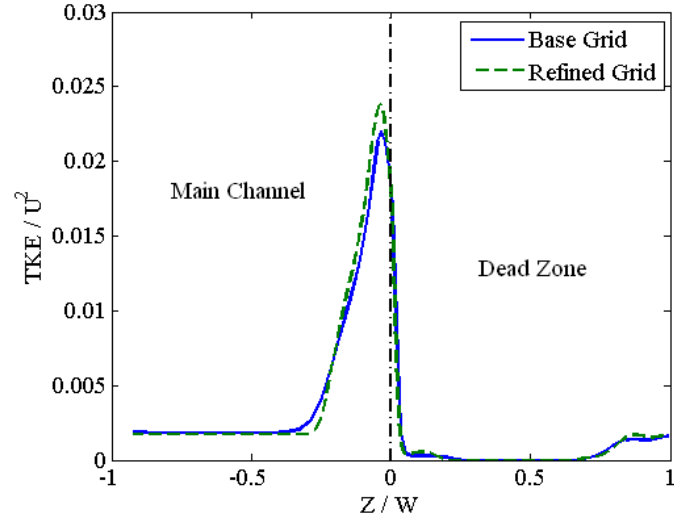
Figure 5.4: TKE profile in the spanwise direction for the base and refined grids. TKE is taken at the free surface and on the centerline of the 5th dead zone in the series using the Uijttewaal geometry.

experimental work done by Uijttewaal et al. [41] and the simulations of McCoy et al. [30]. Figures 5.5 and 5.6 show that the current RANS studies are a good match to the RANS studies done by McCoy. However, there are significant differences between the RANS and experimental results. McCoy's LES results match the experimental results better. The width of the mixing layer is under predicted by the RANS results and the TKE is over predicted.
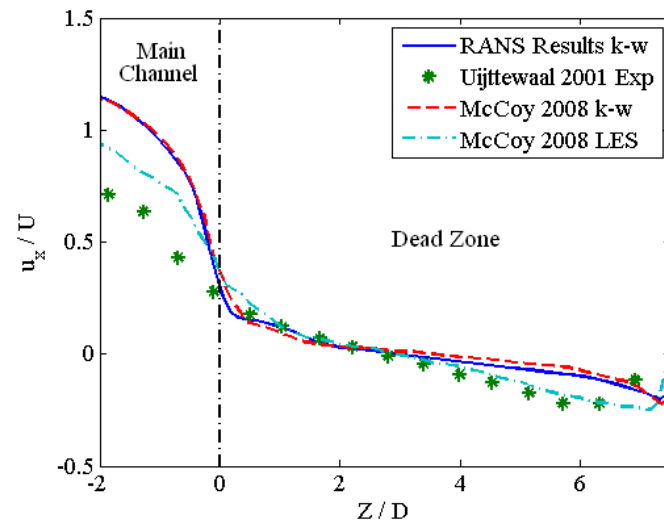
Figure 5.5: Streamwise velocity profile in the spanwise direction for the Uijttewaal geometry comparing the current RANS simulations, experimental work by Uijttewaal et al. [41], and simulations by McCoy et al. [30]. All data is collected at the free surface and X=6 m (in the 6th dead zone).
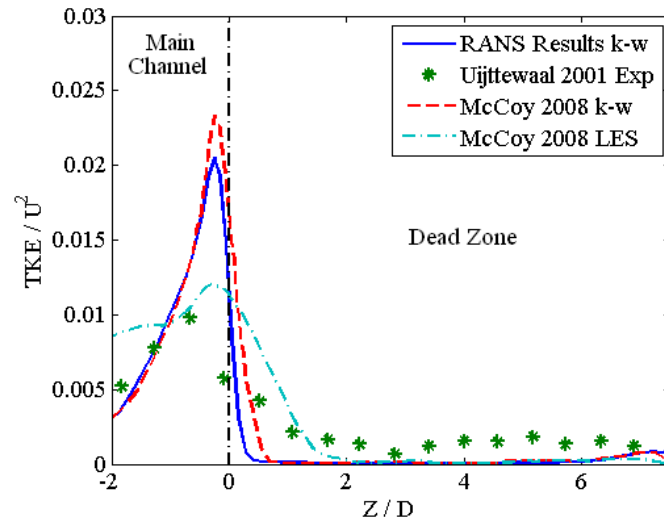
Figure 5.6: TKE profile in the spanwise direction for the Uijttewaal geometry comparing the current RANS simulations, experimental work by Uijttewaal et al. [41], and simulations by McCoy et al. [30]. All data is collected at the free surface and X=6.1 m (in the 6th dead zone).

5.4 Series Results

For a regular series of dead zones, it is important to understand how the properties of the dead zone develop in the series. With enough dead zones in series, it is expected that the shear layer will eventually become fully developed. That is to say that the time scales of exchange will become independent of dead zone rank. Figure 5.7(a) shows how the streamwise velocity varies with streamwise position. By the fourth dead zone, the velocity profile has become periodic with dead zone rank. The TKE profile, shown inFigure 5.7(b), is nearly developed by the fourth dead zone.

Several simulations were also run for the Weitbrecht geometry with variations in dead zone length and average velocity. Figures 5.9(a), 5.9(b), and 5.9(c) show the flow patterns in a fully developed dead zone for different dead zone lengths. For large lengths, the dead zone has one main eddy that is centered slightly downstream of the dead zone center. There is a secondary eddy in the upstream corner of the dead zone. The secondary eddy has significantly less momentum than the primary eddy. As the dead zone length is decreased, the secondary eddy gets smaller and eventually vanishes around a length equal to 0.65 m. As the length is decreased further, the main eddy separates into two eddies stacked in the spanwise direction. Figures 5.8(a) and 5.8(b) show the effect of changes in the average velocity on the flow distribution. The velocity has little effect on the size or location of the primary or secondary eddy. The changes in flow structure can be classified based on the aspect ratio of the dead zone, defined as $\frac{W}{L}$. For aspect ratios less than one,
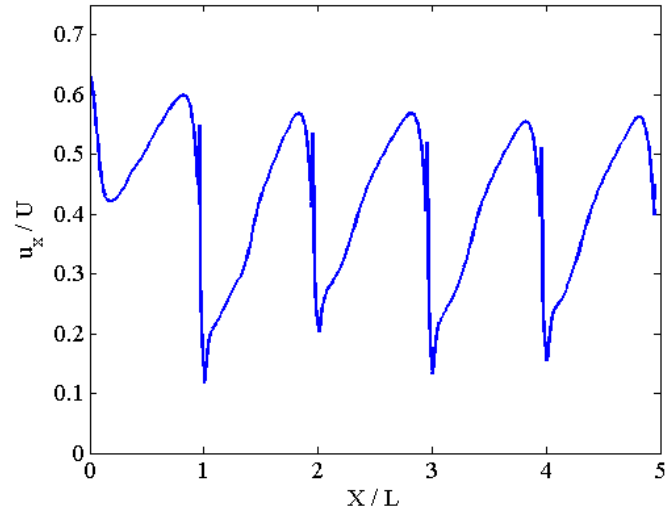
(a) Streamwise velocity
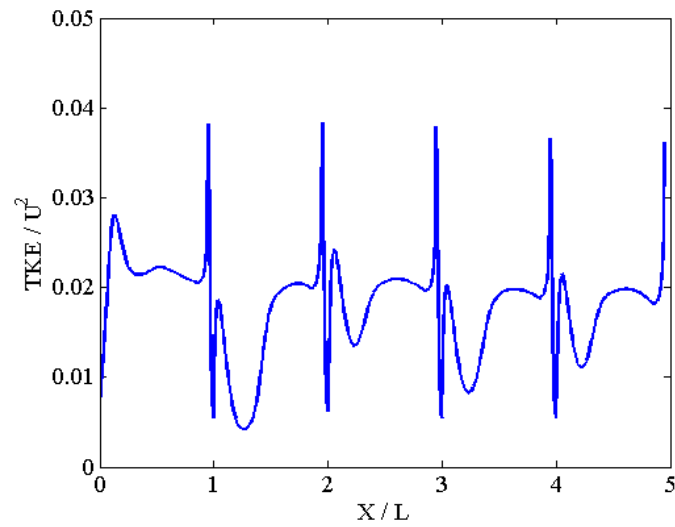
(b) TKE

Figure 5.7: Flow quantities as a function of streamwise position for the refined grid. Data is collected at the free surface on the line that separates the dead zones from the main channel. The developing shear layer is shown for five dead zones.

there is a centrally located primary eddy with a secondary eddy possible in the upstream corner. Large aspect ratios cause multiple eddies to form in a stacked configuration.

(a) U=0.16 $\frac{\text{m}}{\text{s}}$ (b) U=0.20 $\frac{\text{m}}{\text{s}}$
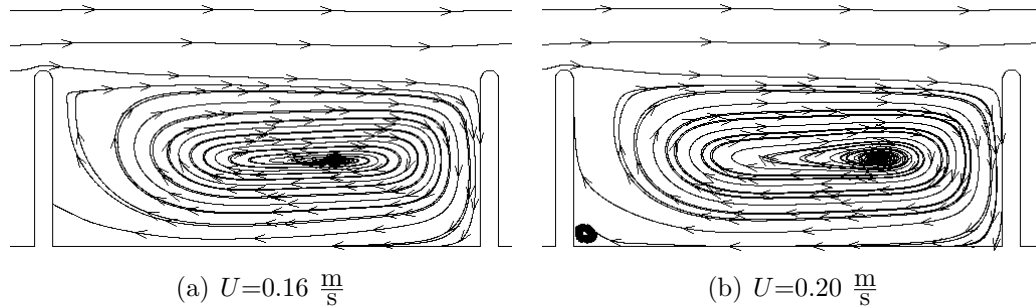
Figure 5.8: Streamlines at the free surface in a dead zone after the shear layer is fully developed for two different average velocities using the Weitbrecht geometry.

(a) L=1.25 m   (b) L=0.65 m   (c) L=0.25
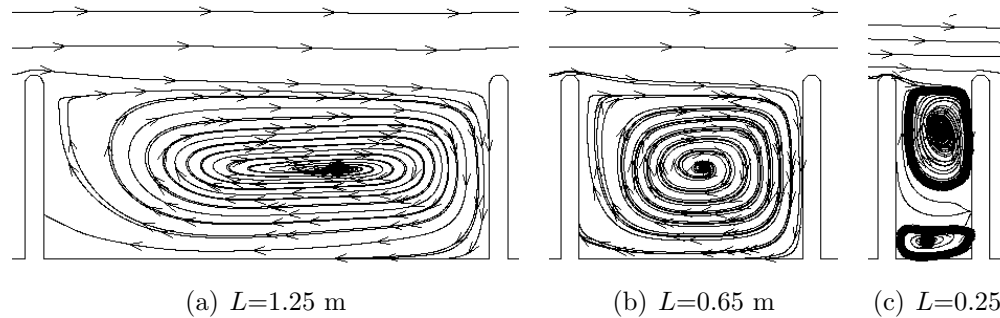
Figure 5.9: Streamlines at the free surface in a dead zone after the shear layer is fully developed for three different lengths using the Weitbrecht geometry.

A quantitative analysis of the time scales in a dead zone also shows a dependence on the aspect ratio. A useful way to describe the exchange process is by plotting a ratio of time scales vs. the aspect ratio, a geometric ratio. The time scales selected are τ_L and T_{conv}. These quantities make a ratio of the flushing time of the dead zone to the time it takes a fluid particle to travel past the dead zone.

Figure 5.10 is a plot of the ratio of time scales to the aspect ratio for these RANS results as well as the experimental results of Weitbrecht et al. [46] and Uijttewaal et al. [41]. Weitbrecht conducted both particle tracking velocimetry, PTV, and dye concentration, PCA, studies.
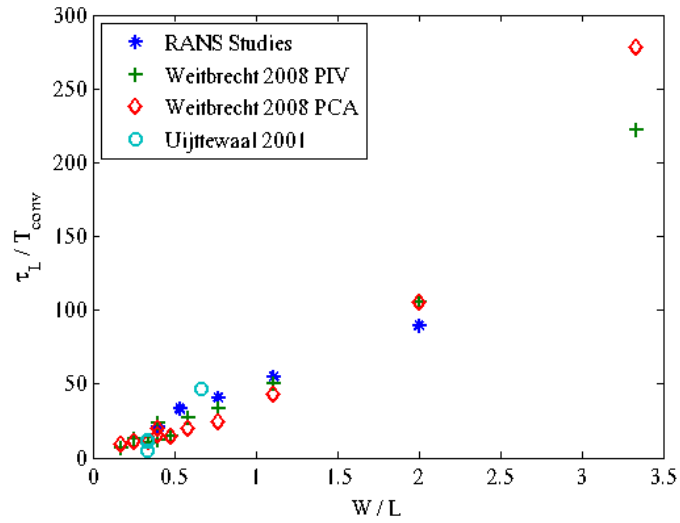
Figure 5.10: Plot of the ratio of the Langmuir to convective time scales vs. the aspect ratio for series of dead zones. Experimental results from Uijttewaal et al. [41] and Weitbrecht et al. [46] are included.

5.5   Single Geometry and Grid

A regular series of dead zones can represent some natural systems well. However, dead zones in typical streams are usually isolated. For this reason, additional simulations were conducted on a single dead zone geometry that is a hybrid of the Weitbrecht and Uijttewaal series geometries. The single dead zone is the cavity

type like the Uijttewaal geometry, but has a constant depth like the Weitbrecht geometry. Figure 5.11 is a plan view of the geometry. Various cases were run for different widths, lengths, depths, and velocities. Table 5.4 lists the different cases run. The grid used is shown in Appendix D and has grid spacing smaller than the refined Uijttewaal series grid. The minimum and maximum grid spacing is in Appendix D. There are 1.46 million cells in the base case grid.
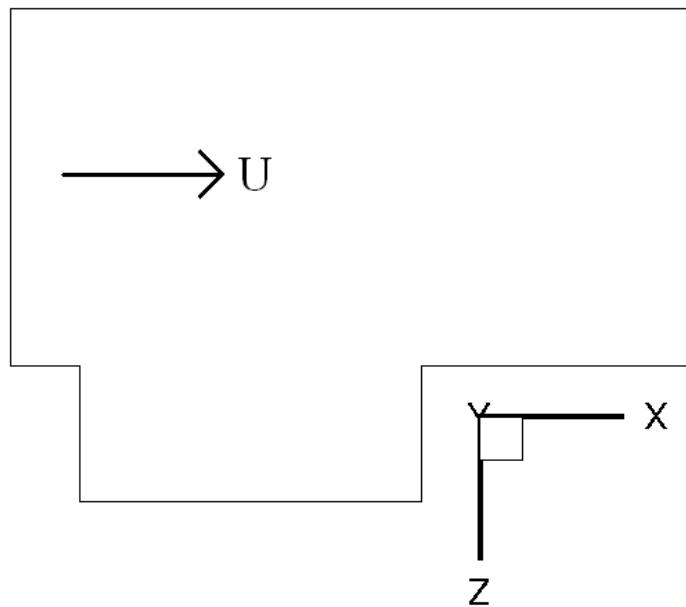
Figure 5.11: Plan view of the single dead zone geometry. The depth is uniform in the main channel and dead zone.

Table 5.4: Different dead zones parameters used in the single dead zone cases.

Case	W [m]	L [m]	D [m]	U [$\frac{m}{s}$]
Base	0.5	1.25	0.046	0.221
2	0.5	1.45	0.046	0.221
3	0.5	1.05	0.046	0.221
4	0.5	0.85	0.046	0.221
5	0.5	0.65	0.046	0.221
6	0.5	0.55	0.046	0.221
7	0.5	0.45	0.046	0.221
8	0.5	1.25	0.046	0.248
9	0.5	1.25	0.046	0.193
10	0.5	1.25	0.046	0.165
11	0.5	1.25	0.046	0.110
12	1.25	1.25	0.046	0.221
13	1	1.25	0.046	0.221
14	0.75	1.25	0.046	0.221
15	0.5	1.25	0.092	0.221
16	0.5	1.25	0.063	0.221
17	0.5	1.25	0.023	0.221

5.6   Single Dead Zone Results

The steady velocity field and transient concentration curve are stored for each of the cases listed in Table 5.4. The general flow structures are similar to the dead zone series results. The low aspect ratio cases have a primary eddy with a secondary eddy in the upstream corner. For aspect ratios around one, the secondary eddy disappears. The largest aspect ratio studied is 1.1 and does not show the stacked eddy configuration.

For the series results, Figure 5.10 showed a clear trend when plotting the ratio of time scales vs. the aspect ratio. The aspect ratio was varied by changing just the

dead zone length. Figure 5.12 is a plot of the same time scale ratio. This figure uses cases that changed the aspect ratio by varying both the length and width of the dead zone. Both the length and width cases show a nearly linear trend, but with different slopes. This suggests that the aspect ratio does not entirely determine the ratio of time scales for a single dead zone.
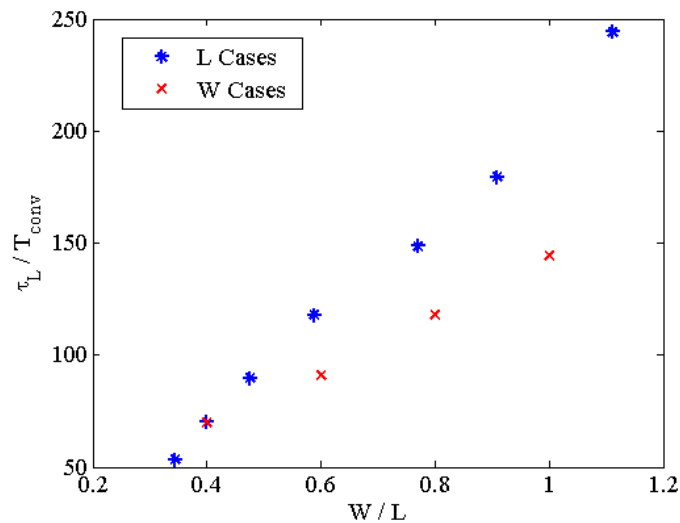
Figure 5.12: Plot of the ratio of the Langmuir to convective time scales vs. the aspect ratio for single dead zone. Only cases varying L and W are shown.

Section 3.1 details the dimensional analysis of a dead zone system. This analysis found that a nondimensional quantity, such as the time scale ratio, should depend on four geometric ratios and one Reynolds number. For these cases, the depth is constant so h_E and h_D can be removed. This leaves two geometric ratios and one Reynolds number. It is also assumed that the time scale ratio will be of the power law form shown in Equation 5.2. Using four independent cases, a system of equations can be generated to solve for the four constants, a, b, c, and d. The

constants are solved for all the possible combinations of independent cases and then averaged. Equation 5.3 shows the resulting function. The geometric ratios can be combined with the Reynolds number and rounded to the nearest whole number. This gives $\frac{W^6 D^4}{L^9}$ as an effective length scale of the dead zone. Figure 5.13 shows that this effective length scale collapses the data for all the cases. The exponents in the effective length scale determine the importance of each parameter. At this time, the exact values of these exponents have no physical or analytical explanation. This correlation can be recast into an expression for the exchange coefficient, k, as shown in Equation 5.4.

$$\frac{\tau_L}{T_{conv}} = a \left(\frac{W}{L}\right)^b \left(\frac{W}{D}\right)^c \left(\frac{WU}{\nu}\right)^d \tag{5.2}$$

$$\frac{\tau_L}{T_{conv}} = 156.9 \left(\frac{W}{L}\right)^{1.28} \left(\frac{W}{D}\right)^{-0.56} \left(\frac{WU}{\nu}\right)^{0.14} \approx 157 \left(\frac{W^6 D^4}{L^9} \frac{U}{\nu}\right)^{\frac{1}{7}} \tag{5.3}$$

$$k = \frac{1}{157} \left(\frac{D^4}{WL^2} \frac{U}{\nu}\right)^{-\frac{1}{7}} \tag{5.4}$$

In addition to the velocity data, transient passive scalar analyses were run for each case. Figure 5.14 is a plot of the concentration for the base case after 5000 s. The maximum concentration in the plot is 0.03 as most of the scalar has left the dead zone. The concentration quickly drops in the circulating region at the perimeter of the primary eddy. The core region of the primary eddy has slow moving fluid and low TKE values. This region stays at a high concentration for
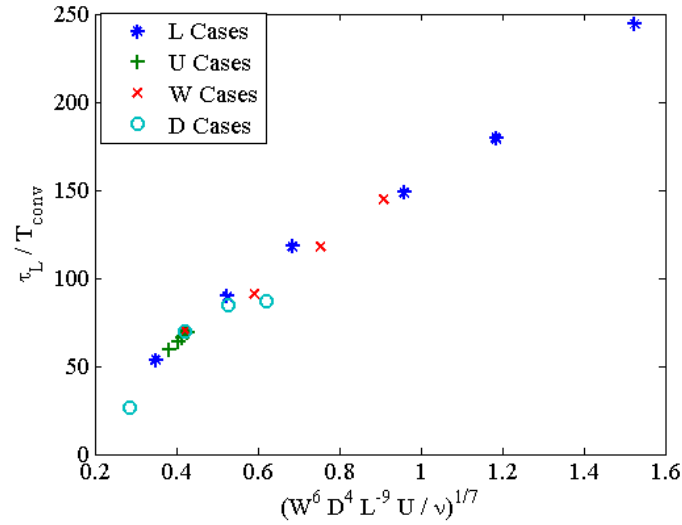
Figure 5.13: Plot of the ratio of the Langmuir to convective time scales vs. an empirically derived nondimensional parameter that includes geometric and flow parameters.

a longer period of time. The normalized volume averaged concentration in the dead zone, C_{DZ}, can be calculated at each time step in the simulation. Figure 5.15 shows a typical concentration plot. The normalized concentration starts at one and decreases in an exponential fashion towards zero concentration. Figure 5.16 shows how the time scale T develops over time. Initially, T is equal to τ_L. As time progresses, T increases and eventually settles to the late time time scale, T_0. The dead zone clearly has multiple time scales and would not be adequately modeled using the first order model.

Figure 5.14: Contour of the concentration within the dead zone for the base single dead zone case. The dark region represents higher concentration.
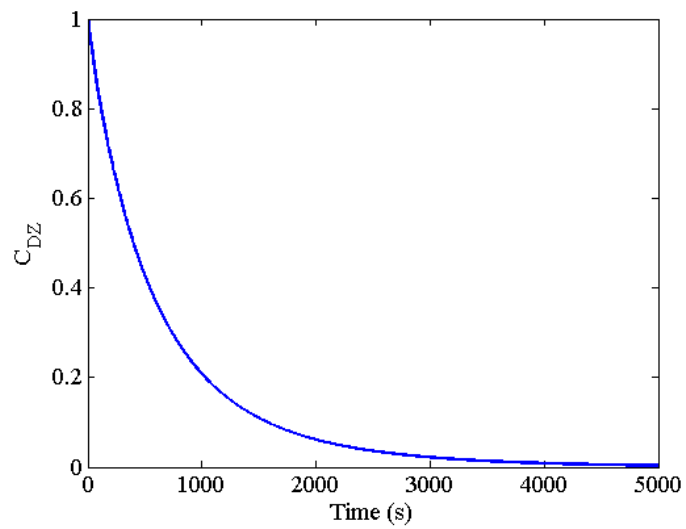
Figure 5.15: Plot of the normalized dead zone concentration vs. time for the base case single dead zone geometry.
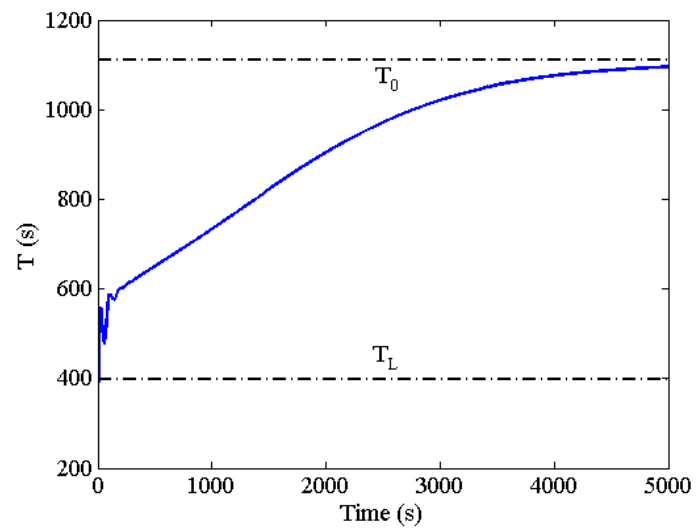
Figure 5.16: Plot of the instantaneous time scale, T, vs. time for the base single dead zone case. τ_L and T_0 are shown for reference.

5.7   Two Region Model

Due to finding multiple time scales in the scalar simulation, the single dead zone results are a good candidate for the two region model. Figure 5.1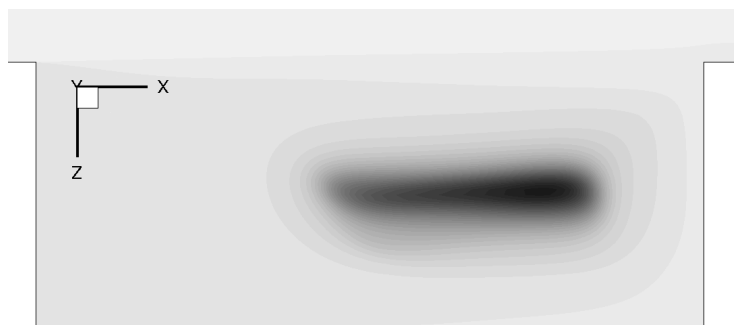7 shows a plot of the two region model fit to the base case RANS simulation results. The two region model fits extremely well throughout the time series. The average percent error for the base case is 0.71%. Table 5.5 lists the fit parameters τ_p, τ_s, and k_3 for all the single dead zone cases. The average error for all the cases is 0.64% with a maximum error of 1.15%. Ideally, the model parameters could also be scaled
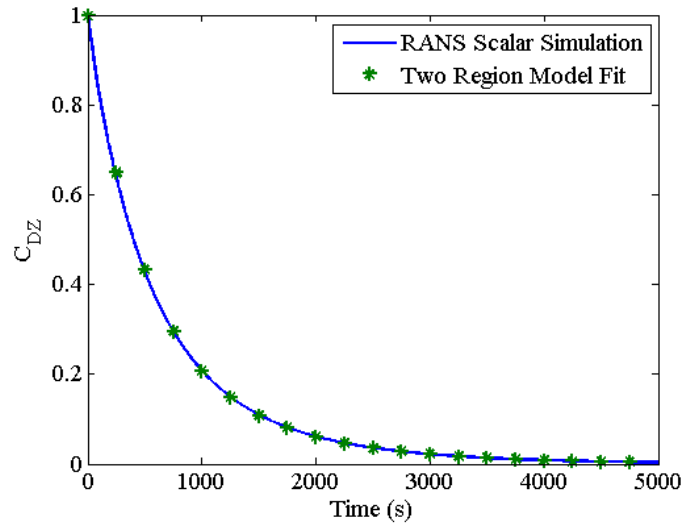
Figure 5.17: Plot of the dead zone concentration for the base single dead zone case. Symbols are from fitting the two region model to the concentration plot. The average error between the two is 0.71%.

based on geometric and flow conditions. However, the model parameters do not conform to the assumed power law form or many other forms tried. Therefore, the two region model can only be applied a posteriori to simulated or experimental

Table 5.5: Results from fitting the two region model to the single dead zone cases. Model parameters τ_p, τ_s, and k_3 are shown as well as the average percent error.

Case	W [m]	L [m]	D [m]	U [$\frac{\text{m}}{\text{s}}$]	τ_p [m]	τ_s [m]	k_3	% Error
Base	0.5	1.25	0.046	0.221	457.4	1086.3	0.669	0.71%
2	0.5	1.45	0.046	0.221	372.7	808.5	0.350	0.77%
3	0.5	1.05	0.046	0.221	408.0	1148.0	0.637	0.53%
4	0.5	0.85	0.046	0.221	410.6	1275.1	0.691	0.82%
5	0.5	0.65	0.046	0.221	414.5	1331.9	0.747	1.15%
6	0.5	0.55	0.046	0.221	403.3	1115.3	0.745	0.96%
7	0.5	0.45	0.046	0.221	347.7	711.4	0.520	0.40%
8	0.5	1.25	0.046	0.248	402.1	909.1	0.664	0.74%
9	0.5	1.25	0.046	0.193	502.8	1262.1	0.686	0.76%
10	0.5	1.25	0.046	0.165	584.4	1449.0	0.645	0.75%
11	0.5	1.25	0.046	0.110	593.6	1643.6	0.290	0.60%
12	1.25	1.25	0.046	0.221	838.2	4767.9	0.549	0.40%
13	1	1.25	0.046	0.221	724.3	4123.8	0.593	0.60%
14	0.75	1.25	0.046	0.221	608.0	3284.0	0.674	0.69%
15	0.5	1.25	0.092	0.221	69.4	571.0	0.060	0.06%
16	0.5	1.25	0.069	0.221	99.0	597.7	0.086	0.22%
17	0.5	1.25	0.023	0.221	372.1	1243.4	0.428	0.82%

results.

There are some useful trends that can be taken from the model results. As the velocity is increased, both τ_p and τ_s decrease while the weighting factor k_3 stays relatively unchanged. This is somewhat intuitive as increasing the velocities throughout the system will decrease all time scales. A constant k_3 value indicates that the size and flow properties of the secondary region are somewhat independent of velocity. This trend is consistent with the qualitative flow structure results from the series simulations. The width cases also show a clear trend of the time scales increasing with an increasing width. This is most likely due to increasing the

perimeter of the dead zone and thus increasing the time it takes a fluid particle to circulate around the entire dead zone. k_3 tends to decrease with an increasing width. This trend indicates that the influence of the secondary region is increasing for larger widths possibly due to increasing the volume of the secondary region relative to the primary region.

The two region model can also be applied to experimental concentration curves. Figure 5.18 shows three experimental concentration curves measured by Jackson et al. [14] in dead zones of small natural streams. The two region model does a reasonable job of approximating the experimental results with average errors of 14.3%, 12.5%, and 6.29%. Most of the error occurs in the early time. This trend may be due to slightly different initial conditions. The model assumes the dead zone is initially at a uniform distribution. The experimental results were obtained by injecting concentration into the dead zone until a steady condition is reached. Then injecting is stopped and the concentration curve measured. The steady state condition could have significant gradients in concentration and would alter the early time behavior.
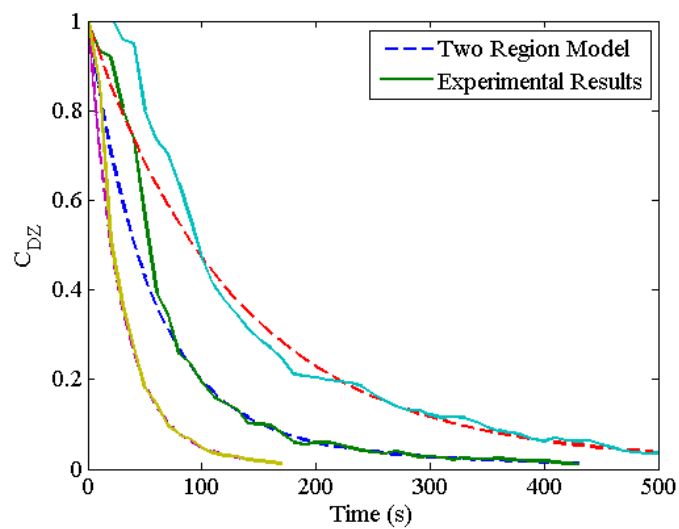
Figure 5.18: Three experimental concentration plots by Jackson et al. [14] fit with the two region model.

Chapter 6: LES Cases

6.1 Geometry and Grids

The LES cases use a single dead zone version of the geometry used by Uijttewaal. This geometry has a cavity type dead zone with a non-uniform depth. The single dead zone is 1.125m long, 0.75 m wide, and has an average velocity of 0.35 $\frac{m}{s}$. The main channel depth is 0.1 m. The dead zone has an average depth of 0.05 m and the depth at the dead zone main channel interface is 0.06 m. Figures 5.1(a) and 5.1(b) show plan view and cross sectional diagrams of this geometry except this geometry uses only one dead zone.

The LES solver does not use wall models and therefore the grid used must resolve the boundary layers on both the channel bottom and the side walls. Two grids were generated to examine what refinement is necessary. Each grid uses structured hexagonal cells in the dead zone and shear layer. Triangular prism cells were used in the main channel to reduce the cell count. The grid spacing is highly stretched near the wall to reduce the cell count, but still resolves the boundary layer. Table 6.1 shows the grid spacing used for both the coarse and fine grids in meters and wall units. Appendix E has detailed figures of the grids used. The coarse grid uses 1.54 million cells compared to the fine grid's 10.4 million.

Table 6.1: Grid spacings for the coarse and refined LES grids in the dead zone and shear layer in meters and wall units.

	Min [m]	Max [m]		Min	Max
Coarse Grid					
ΔY	9.24E-5	0.0104	ΔY^+	1.78	200.75
ΔX	9.24E-5	0.0104	ΔX^+	1.78	200.75
ΔZ	9.24E-5	0.0129	ΔZ^+	1.78	249.01
Refined Grid					
ΔY	4.62E-5	0.0052	ΔY^+	0.89	200.75
ΔX	4.62E-5	0.0104	ΔX^+	0.89	200.75
ΔZ	4.62E-5	0.0064	ΔZ^+	0.89	123.54

6.2 Solution Procedure

The solution procedure for the LES cases is similar to RANS case. First, a fully developed inlet condition is simulated using a periodic channel and saved. The actual dead zone geometry is simulated using the inlet condition and the stationary velocity field is found. The main difference is that LES is a time accurate model and thus all simulations are transient.

The periodic channel is simulated using a constant mass flow rate condition. A constant mass flow rate is enforced by adding a uniform body force to the fluid in the channel. The body force is calculated from a momentum balance of the channel. Momentum needs to be added through the body force to make up the difference between the current total momentum and the desired momentum and to overcome the momentum lost to shear force at the walls. When the periodic channel has reached a stationary state, the body force will be steady and balance

the shear force.

Another important consideration is adding perturbations to the periodic channel. These perturbations will develop into turbulence. Without adding perturbations, the flow will take a long time to transition to a fully turbulent flow. The perturbations are added to the initial velocity condition. Sinusoidal perturbations were added with a magnitude equal to 40% of the average velocity. Linear damping of the perturbations was used near the wall to ensure the perturbations match the no-slip condition. The channel was assumed to be fully developed when the body force term reached a steady state. The fully developed inlet was saved from a cross sectional plane of the channel at every tenth time step. Data was saved for a period of time approximately equal to three flow-through times for the actual geometry.

The saved time resolved inlet condition was used as the inlet boundary condition for the actual dead zone geometry. The inlet data is interpolated in both time and space to the dead zone grid. When the simulation reaches the end of the time series of inlet data, it wraps around to the beginning of the inlet data set. The dead zone simulation is then allowed to run until it has reached a stationary state, when the time averaged velocities are not changing appreciably. The average velocity and normal components of the Reynolds Stresses are saved at each time step. The averaged quantities are then reset and the simulation is allowed to run until the averages reach steady values. The time step used for the refined grid is 2.5E-5 seconds. No passive scalar simulations were run with LES due to the computational expense of running the simulation for 200+ seconds.

6.3   LES Results

The average velocity fields for both the coarse and refined grids were stored and compared to a RANS simulation that uses the same grid as the coarse LES. Figure 6.1 shows a velocity profile in the spanwise direction. This profile shows that the coarse and refined LES give similar results. The refined case predicts slightly lower velocities in the shear region and a more constant slope inside the dead zone. The RANS velocity profile is significantly different from both LES cases. The shear layer is smaller and there is zero velocity region near the center of the dead zone.
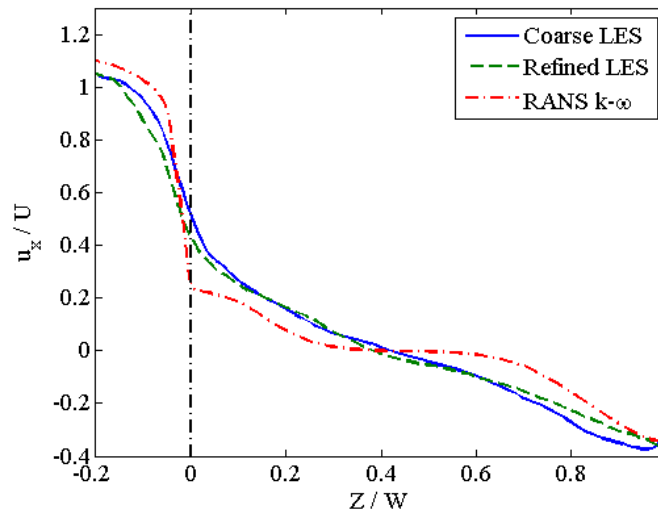

Figure 6.1: Plot comparing the streamwise velocity profile in the spanwise direction for both LES grids to a RANS simulation on the coarse grid. The dashed vertical line represents the main channel-dead zone interface. Data is collected at the free surface and on the X=0.4m line.

The current LES can also be compared to the experimental results by Uijttewaal et al. [41] and the LES by McCoy et al. [30]. While Uijttewaal and McCoy

use a series instead of a single geometry, the first dead zone should be mostly unaffected by downstream dead zones. Figure 6.2 shows a velocity profile in the spanwise direction comparing the two LES simulations with the experimental results. The current LES case matches the experiments quite well in the dead zone. The experiments show a lower velocity in the shear layer. There are differences between the two LES simulations probably due to a more refined grid in this work or the length of time over which the velocity was averaged.
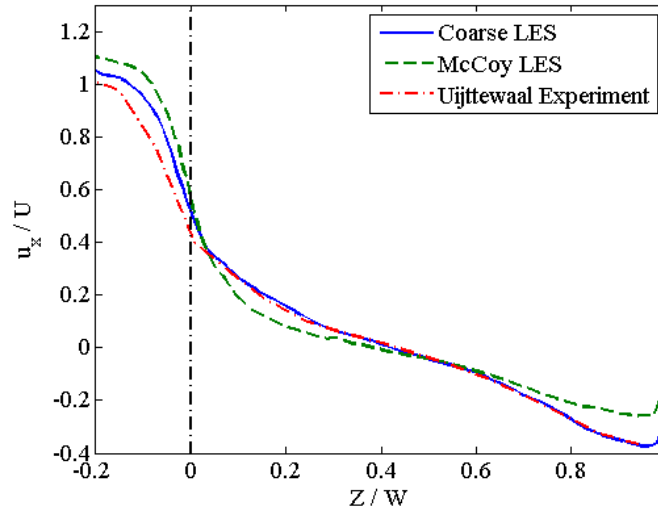

Figure 6.2: Plot comparing the streamwise velocity profile in the spanwise direction for this LES study, LES by McCoy et al. [30], and experiments by Uijttewaal et al. [41]. The dashed vertical line represents the main channel-dead zone interface. Data is collected at the free surface and on the X=0.4m line.

Figure 6.3 shows streamlines for the time averaged flow field. The general flow structure looks similar to the RANS studies shown in Figure 5.9(b) for an aspect ratio near one. The primary eddy in the LES is slightly more oval. However, the differences in depth, channel velocity, and series vs. single geometry could

contribute to this difference.

The exchange velocity between the dead zone and main channel makes up τ_L. Figure 6.4 is a contour plot of the local exchange velocity at the interface between the dead zone and the main channel. There are distinct regions where the time averaged flow is into or out of the dead zone. However, the net flow into the dead zone must be zero to conserve mass. There are strong velocities out of the dead zone near the stagnation region at the downstream corner. There is also a large region of flow into the dead zone near the downstream edge and closer to the bottom of the dead zone. The depth dependence implies that measurements taken near the free surface may not be representative of the entire flow.

LES provide much more turbulence data than RANS simulations. RANS simulations treat turbulence as isotropic as the Reynolds Stresses are modeled by the ratio k and ω, two scalar fields. Figure 6.5 is a contour plot of the $\overline{u'_x u'_x}$ component of the Reynolds Stress tensor. There is a distinct region of increased fluctuations in the shear layer to turbulent structures shed off the upstream corner of the dead zone. The largest fluctuations are where the shear layer stagnates near the downstream corner. Some of the fluctuations begin to recirculate in the dead zone, but dissipate quickly. Similar to the RANS simulation, there is a region near the center of the dead zone with reduced turbulence. However, this region has a more irregular shape compared to the RANS simulation. Appendix F has additional plots of the mean velocity and Reynolds Stress.
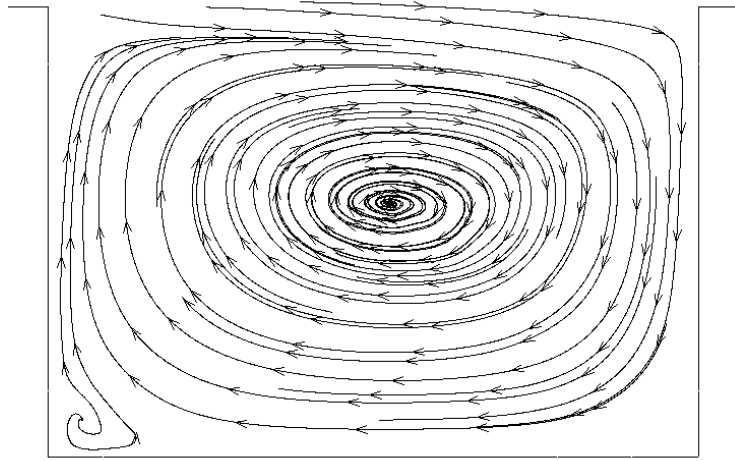
Figure 6.3: Average streamlines at the free surface in the dead zone for the coarse LES grid.
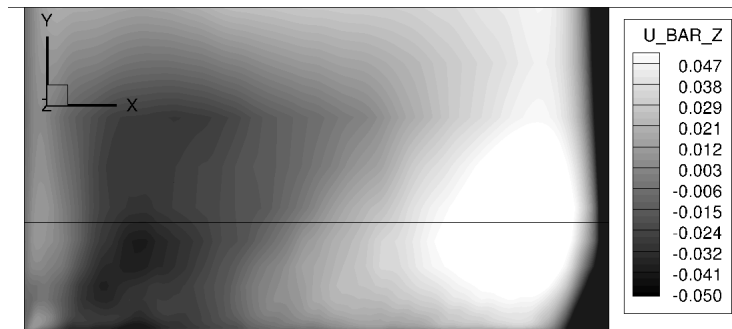

Figure 6.4: Contours of $\frac{\overline{u}_z}{U}$, the time averaged exchange velocity at the interface between the dead zone and main channel for the coarse LES grid. The Y dimension is stretched by a factor of 10.
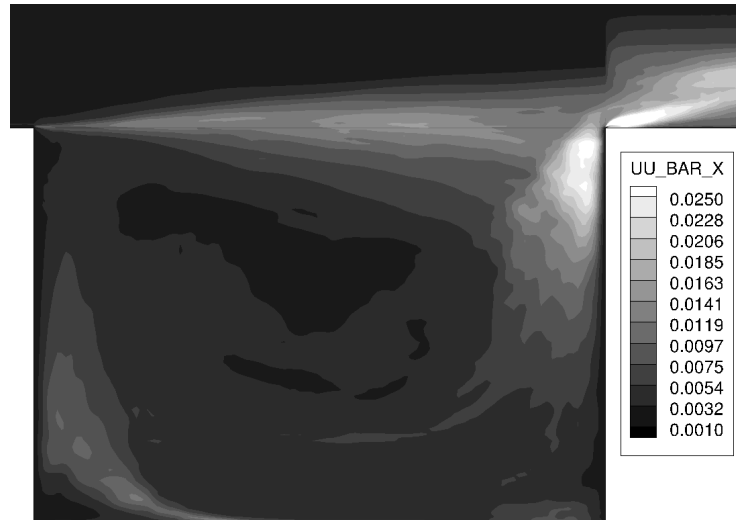
Figure 6.5: Plan view contours of $\overline{\frac{u'_x u'_x}{U^2}}$ at the free surface for the coarse LES grid.

The RANS and LES velocity profiles showed some differences. As a test of how significant these differences are to scalar transport, a RANS passive scalar analysis was run using the time averaged flow field from the LES study. No velocity interpolation was needed as the RANS simulation was also run on the coarse LES grid. With the LES flow field, the RANS simulation was first allowed to calculated k and ω. Then a transient passive scalar study was conducted and compared to an all RANS simulations.

Figure 6.6 shows the time series of both passive scalar studies. The concentration of the RANS case initially decreases more quickly. At later times, the LES concentration eventually becomes less than the RANS case. The two region model was applied to both cases and the resulting parameters are shown in Table 6.2. Both time scales are significantly smaller for the LES case. The LES k_3 value

initially puts little weight on τ_p which explains the slow transport at early time. At late time when τ_s dominates, the concentration decreases faster for the LES case compared to the RANS.
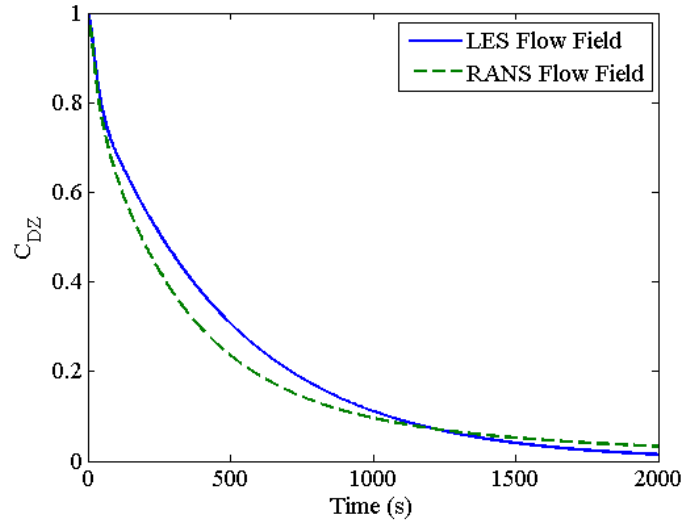

Figure 6.6: Plots of the normalized dead zone concentration vs. time for RANS scalar studies using the time average flow field from LES and RANS. Both simulations use the coarse LES grid.

Table 6.2: Two region parameters, τ_p, τ_s, and k_3, fit to the concentration plots from RANS passive scalar analyses using the mean flow field from LES and RANS. The average percent error between model and simulation is also shown.

	τ_p [s]	τ_s [s]	k_3	% Error
LES	29.56	493.2	0.156	0.39
RANS	226.9	978.1	0.759	3.54

Chapter 7: Conclusions

RANS simulations of series of dead zones were carried out for a range of lengths and average velocities on similar geometries to past experiments. It was determined that the flow is fully developed after four dead zones. This result means that only the first four dead zones need to be studied to get the characteristics of a much longer series. The time averaged velocity field generally matches the experiment with a large eddy at the center of the dead zone with additional eddies depending on the aspect ratio. When $\frac{\tau_L}{T_{conv}}$ is plotted vs. the W/L ratio, the simulations and experiments show an increasing trend. However, most of this data was generated using variable dead zone lengths. For the single dead zone geometry, varying both the width and length showed that $\frac{\tau_L}{T_{conv}}$ depends on more than just the aspect ratio.

This dependence led to additional cases varying the depth and velocity. Nondimensionalizing the results leads to a functional relationship between the relevant nondimensional groups, $\frac{W}{L}$, $\frac{W}{D}$, and Re_W, and the time scale ratio, $\frac{\tau_L}{T_{conv}}$. The nondimensionalization can be interpreted as a Reynolds number with an effective length scale of $\frac{W^6 D^4}{L^9}$. This length scale was determined empirically and therefore the exponents have no physical origin. Using this length scale in a Reynolds number allows τ_L to be predicted from the easily measurable parameters L, W, D, and U. If this type of relationship is found to hold good for irregularly shaped natural dead zones, time intensive tracer experiments would not be needed to get

an estimate of τ_L

The passive scalar simulations showed that the dead zone is not perfectly mixed. The core of the primary eddy retains scalar longer than the perimeter of the eddy. This leads to multiple time scales being present in the dead zone. The first order dead zone model uses a single time scale and is therefore incapable of modeling these results. A two region model was developed that can be fit to the simulated concentration plots with minimal error. The model also represents experimental concentration plots reasonably well despite slightly different initial conditions. The two region model suggests that the time scales within the dead zone increase with increasing width and decreasing velocity.

The LES simulations for a single dead zone matched well to experiments and past LES simulations. The mean velocity distribution in the exchange region shows a strong dependence on depth. This dependence suggests that measurements taken near the free surface are not representative of the depth-averaged values. This limits the effectiveness of surface measurements methods such as tracking floating particles and highlights the need for full field experimental techniques such as particle image velocimetry. While the mean velocity profiles are similar between the RANS and LES studies, there are noticeable differences even for the same grid. These differences were shown to significantly affect passive scalar studies. This result diminishes the quantitative predictive capability of the RANS models for this geometry. However, the trends shown by the RANS simulations serve to guide future LES and experimental studies into the scaling of the transport time scales.

The results discussed in this work are only valid over the range of nondimensional quantities studied. The Re_D values used, 8300-39300, are characteristic of small natural streams. While the Reynolds number dependence on the flow structures was shown to be small, rivers likely have different flow features. The aspect ratio studied are similar to those found in field work by Jackson et al. [14]. Large aspect ratios where the dead zone flow is almost stagnate and small aspect ratios where the shear layer could reattach are not considered. There are additional parameters, such as rough beds, irregularly shaped banks, and high Froude numbers, that need further experimental and computational work to be incorporated into existing dead zone models.

Bibliography

[1] SV Apte, K. Mahesh, P. Moin, and JC Oefelein. Large-eddy simulation of swirling particle-laden flows in a coaxial-jet combustor. *International Journal of Multiphase Flow*, 29(8):1311–1331, 2003.

[2] J.J. Baik, J.J. Kim, and H.J.S. Fernando. A cfd model for simulating urban flow and dispersion. *Journal of Applied Meteorology*, 42(11):1636–1648, 2003.

[3] A. Bellucci, G. Buffoni, A. Griffa, and E. Zambianchi. Estimation of residence times in semi-enclosed basins with steady flows. *Dynamics of atmospheres and oceans*, 33(3):201–218, 2001.

[4] K.E. Bencala and RA Walters. Simulation of solute transport in a mountain pool-and-riffle stream with a kinetic mass transfer model for sorption. *Water Resources Research*, 19(3):732–738, 1983.

[5] B. Biglari et al. Numerical modeling of flow around bridge abutments in compound channel. *Journal of Hydraulic Engineering*, 124:156, 1998.

[6] K. Chang, G. Constantinescu, and S.O. Park. Analysis of the flow and mass transfer processes for the incompressible flow past an open cavity with a laminar and a fully turbulent incoming boundary layer. *Journal of Fluid Mechanics*, 561(4):113–145, 2006.

[7] G. Constantinescu, A. Sukhodolov, and A. McCoy. Mass exchange in a shallow channel flow with a series of groynes: Les study and comparison with laboratory and field experiments. *Environmental fluid mechanics*, 9(6):587–615, 2009.

[8] C. Engelhardt, A. Krüger, A. Sukhodolov, and A. Nicklisch. A study of phytoplankton spatial distributions, flow structure and characteristics of mixing in a river reach with groynes. *Journal of plankton research*, 26(11):1351–1366, 2004.

[9] M. Germano, U. Piomelli, P. Moin, and W.H. Cabot. A dynamic subgrid-scale eddy viscosity model. *Physics of Fluids A: Fluid Dynamics*, 3:1760, 1991.

[10] PE Gill, W. Murray, and A. Saunders. Snopt 5.3 user manual. *Department of Mathematics, University of California, San Diego*, 1994.

[11] C. Gualtieri, P.A.L. Jiménez, and J.M. Rodríguez. Modelling turbulence and solute transport in a square dead zone.

[12] U. Guide. Star-ccm+ version 4.04. 011, 2009.

[13] C. Hinterberger, J. Fröhlich, and W. Rodi. Three-dimensional and depth-averaged large-eddy simulations of some shallow water flows. *Journal of Hydraulic Engineering*, 133:857, 2007.

[14] T.R. Jackson, R. Haggerty, S.V. Sourabh, A. Coleman, and K.J. Drost. The mean residence time of lateral surface transient storage zones in streams. Unpublished manuscript, May 2012.

[15] I. Kimura and T. Hosoda. Fundamental properties of flows in open channels with dead zone. *Journal of Hydraulic Engineering*, 123:98, 1997.

[16] H.P. Kozerski, R. Schwartz, and T. Hintze. Tracer measurements in groyne fields for the quantification of mean hydraulic residence times and of the exchange with the stream. *Acta hydrochimica et hydrobiologica*, 34(3):188–200, 2006.

[17] M. Kurzke, V. Weitbrecht, and G.H. Jirka. Laboratory concentration measurements for determination of mass exchange between groin fields and main stream. In *River Flow*, volume 1, pages 369–376, 2002.

[18] I. Langmuir. The velocity of reactions in gases moving through heated vessels and the effect of convection and diffusion. *Journal of the American Chemical Society*, 30(11):1742–1754, 1908.

[19] L. Larchevêque, P. Sagaut, and O. Labbé. Large-eddy simulation of a subsonic cavity flow including asymmetric three-dimensional effects. *Journal of Fluid Mechanics*, 577(1):105–126, 2007.

[20] C. Leibundgut, U. Speidel, and H. Wiesner. Transport processes in rivers investigated by tracer experiments. *IAHS PUBLICATION*, pages 211–211, 1993.

[21] O. Levenspiel. *Chemical Reaction Engineering: An Introduction to the Design of Chemical Reactors.* John Wiley & Sons, 1967.

[22] K. Lien, JP Monty, MS Chong, and A. Ooi. The entrance length for fully developed turbulent channel flow. In *15th Australasian Fluid Mechanics Conference, The University of Sydney, Ausralia*, 2004.

[23] DK Lilly. A proposed modification of the germano subgrid-scale closure method. *Physics of Fluids A: Fluid Dynamics*, 4:633, 1992.

[24] J.C. Lin and D. Rockwell. Organized oscillations of initially turbulent flow past a cavity. *Aiaa Journal*, 39(6):1139–1151, 2001.

[25] X. Liu and J. Katz. Cavitation phenomena occurring due to interaction of shear layer vortices with the trailing corner of a two-dimensional open cavity. *Physics of fluids*, 20(4):41702–41702, 2008.

[26] K. Mahesh, G. Constantinescu, and P. Moin. A numerical method for large-eddy simulation in complex geometries. *Journal of Computational Physics*, 197(1):215–240, 2004.

[27] G.U. Manual. Version 16.0, pointwise. *Inc., Fort Worth, TX*, 2008.

[28] A. McCoy, G. Constantinescu, and L. Weber. Exchange processes in a channel with two vertical emerged obstructions. *Flow, turbulence and combustion*, 77(1):97–126, 2006.

[29] A. McCoy, G. Constantinescu, and L. Weber. A numerical investigation of coherent structures and mass exchange processes in channel flow with two lateral submerged groynes. *Water resources research*, 43(5):W05445, 2007.

[30] A. McCoy, G. Constantinescu, L.J. Weber, et al. Numerical investigation of flow hydrodynamics in a channel with a series of groynes. *Journal of Hydraulic Engineering*, 134:157, 2008.

[31] P. Moin and SV Apte. Large-eddy simulation of realistic gas turbine combustors. *AIAA J. v44*, 698, 2006.

[32] E.B. Nauman. Residence time theory. *Industrial & Engineering Chemistry Research*, 47(10):3752–3766, 2008.

[33] S. Ouillon and D. Dartus. Three-dimensional computation of flow around groyne. *Journal of Hydraulic Engineering*, 123(11):962–970, 1997.

[34] E. Özsoy, P. Rambaud, A. Stitou, and ML Riethmuller. Vortex characteristics in laminar cavity flow at very low mach number. *Experiments in fluids*, 38(2):133–145, 2005.

[35] R. Rossi and G. Iaccarino. Numerical simulation of scalar dispersion downstream of a square obstacle using gradient-transport type models. *Atmospheric Environment*, 43(16):2518–2531, 2009.

[36] J.L. Santiago, A. Martilli, and F. Martín. Cfd simulation of airflow over a regular array of cubes. part i: Three-dimensional simulation of the flow and validation with wind-tunnel measurements. *Boundary-layer meteorology*, 122(3):609–634, 2007.

[37] E. Shams and S.V. Apte. Prediction of small-scale cavitation in a high speed flow over an open cavity using large-eddy simulation. *Journal of Fluids Engineering*, 132:111301, 2010.

[38] J. Smagorinsky. General circulation experiments with the primitive equations. *Monthly weather review*, 91(3):99–164, 1963.

[39] Y. Tominaga and T. Stathopoulos. Turbulent schmidt numbers for cfd analysis with various types of flowfield. *Atmospheric Environment*, 41(37):8091–8099, 2007.

[40] M. Tritthart, M. Liedermann, and H. Habersack. Modelling spatio-temporal flow characteristics in groyne fields. *River Research and Applications*, 25(1):62–81, 2009.

[41] WSJ Uijttewaal, D. Lehmann, and A. Van Mazijk. Exchange processes between a river and its groyne fields: Model experiments. *Journal of Hydraulic Engineering*, 127:928, 2001.

[42] E.M. Valentine and I.R. Wood. Longitudinal dispersion with dead zones. *Journal of the Hydraulics Division*, 103(9):975–990, 1977.

[43] E.M. Valentine and I.R. Wood. Dispersion in rough rectangular channels. *Journal of the Hydraulics Division*, 105(12):1537–1553, 1979.

[44] W. Van Balen, WSJ Uijttewaal, and K. Blanckaert. Large-eddy simulation of a mildly curved open-channel flow. *Journal of Fluid Mechanics*, 630(1):413–442, 2009.

[45] V. Weitbrecht and G.H. Jirka. Flow patterns and exchange processes in dead zones of rivers. In *PROCEEDINGS OF THE CONGRESS-INTERNATIONAL ASSOCIATION FOR HYDRAULIC RESEARCH*, pages 439–445, 2001.

[46] V. Weitbrecht, S.A. Socolofsky, G.H. Jirka, et al. Experiments on mass exchange between groin fields and main stream in rivers. *Journal of Hydraulic Engineering*, 134:173, 2008.

[47] D.C. Wilcox. Reassessment of the scale-determining equation for advanced turbulence models. *AIAA journal*, 26(11):1299–1310, 1988.

[48] H. Yao, RK Cooper, and S. Raghunathan. Numerical simulation of incompressible laminar flow over three-dimensional rectangular cavities. *Journal of fluids engineering*, 126:919, 2004.

[49] M.F.M. Yossef and H.J. de Vriend. Flow details near river groynes: Experimental investigation. *Journal of Hydraulic Engineering*, 137:504, 2011.

APPENDICES

Appendix A: k-ω Equations

The turbulent kinetic enery, k, and specific dissipation, ω equations are shown in Equations A.1 and A.2. The model parameters used are shown in Table A.1. The k-ω model was selected for its computational efficiency, validation history, and similarity to past work. This model introduces the two additional transport equations shown above which adds compuatational expense. However, this model is significantly less expensive than another popular model, the Reynolds stress model which adds six equations. The k-ω and k-ϵ two equation models are widely used and have been tuned and validated for many different applications including separated flows similar to a dead zone. Of these two models, the k-ω model was chosen to match the work done by McCoy et al. [30]. Once this solver was validated against McCoy's work, the same model was used for the rest of the studies for consistency.

$$\overline{u}_j \frac{\partial k}{\partial x_j} = \tau_{ij} \frac{\partial \overline{u}_i}{\partial x_j} - \beta^* k \omega + \frac{\partial}{\partial x_j} \left[\left(\nu + \sigma^* \nu_T \right) \frac{\partial k}{\partial x_j} \right] \tag{A.1}$$

$$\overline{u}_j \frac{\partial \omega}{\partial x_j} = \alpha \frac{\omega}{k} \tau_{ij} \frac{\partial \overline{u}_i}{\partial x_j} - \beta \omega^2 + \frac{\partial}{\partial x_j} \left[\left(\nu + \sigma^* \nu_T \right) \frac{\partial \omega}{\partial x_j} \right] \tag{A.2}$$

Table A.1: Table of the model parameters used in the k-ω turbulence model.

Constant	Value
α	$\frac{13}{25}$
β	$\frac{9}{125}$
β^*	0.09
σ^*	0.5

Appendix B: Uijttewaal Grids
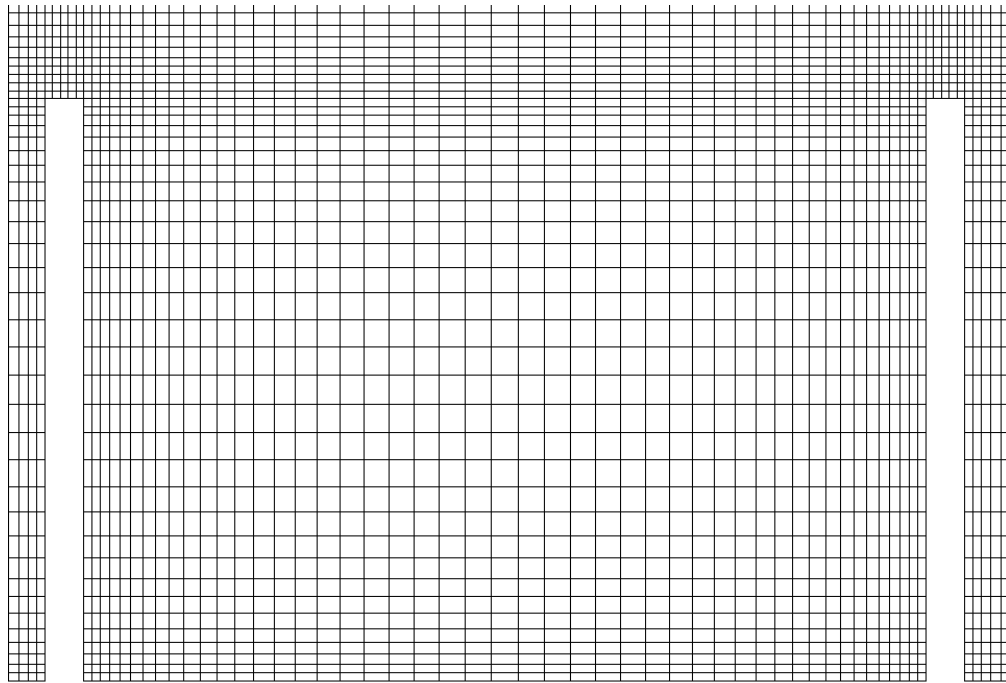

Figure B.1: Cross section of the Uijttewaal grid.

Figure B.2: Detailed plan view of the Uijttewaal grid used in a dead zone.
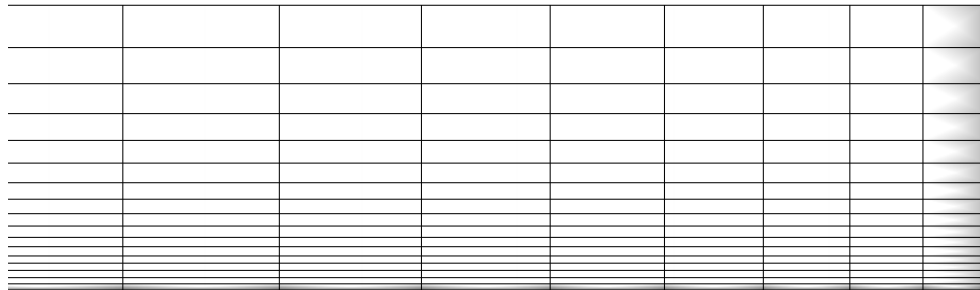
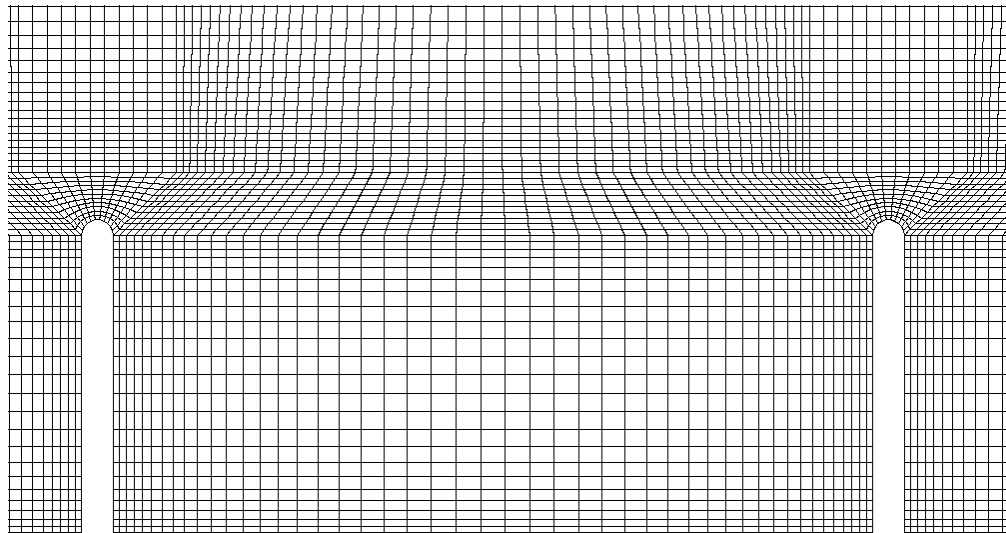# Appendix C: Weitbrecht Grids

Figure C.1: Cross section of the Weitbrecht grid.

Figure C.2: Detailed plan view of the Weitbrecht grid used in the dead zone.

Appendix D: Single Grid

Table D.1: Table of the grid spacing for the single dead zone geometry in the dead zone and shear layer in both meters and wall units.

	Min [m]	Max [m]		Min	Max
ΔY	9.24E-05	0.0052	ΔY^+	1.06	59.60
ΔX	9.24E-05	0.0104	ΔX^+	1.06	119.20
ΔZ	9.24E-05	0.0104	ΔZ^+	1.06	119.20
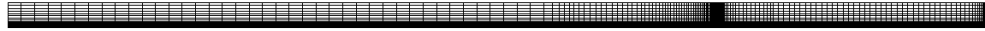
Figure D.1: Cross section of the single geometry grid.
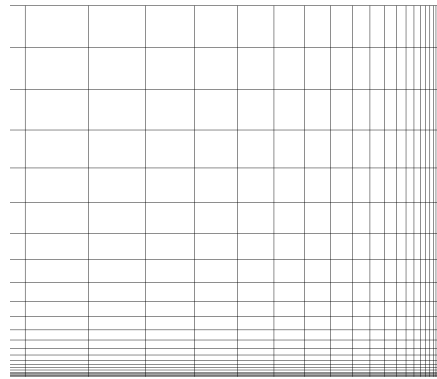
Figure D.2: Detailed view of the cross section of the dead zone corner for the single geometry grid.
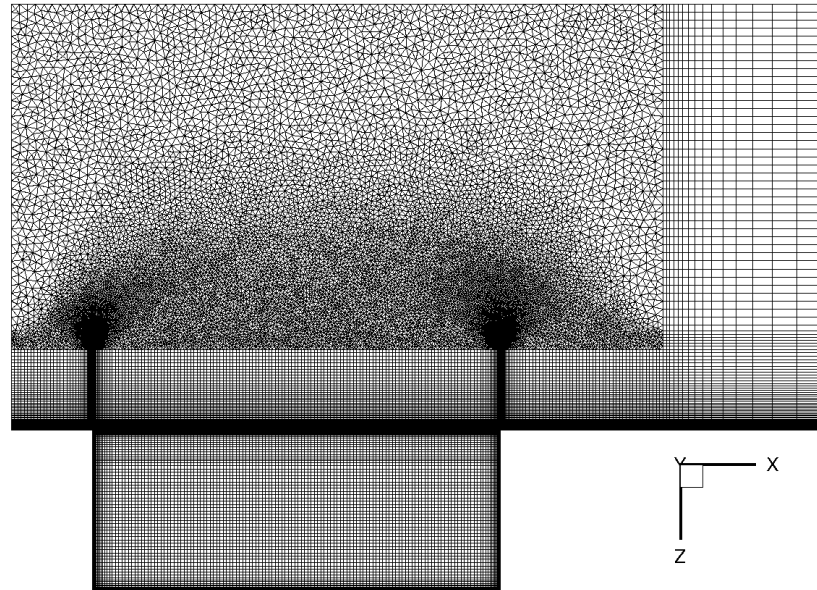
Figure D.3: Plan view of the grid used in the single dead zone cases.
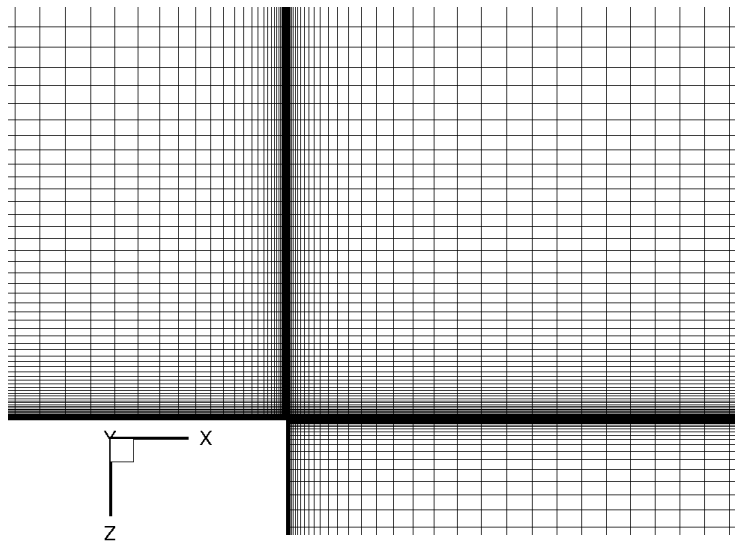
Figure D.4: Detailed plan view of the upstream corner of the dead zone for the grid used in the single dead zone cases.

Appendix E: LES Grid
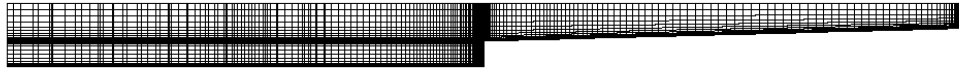
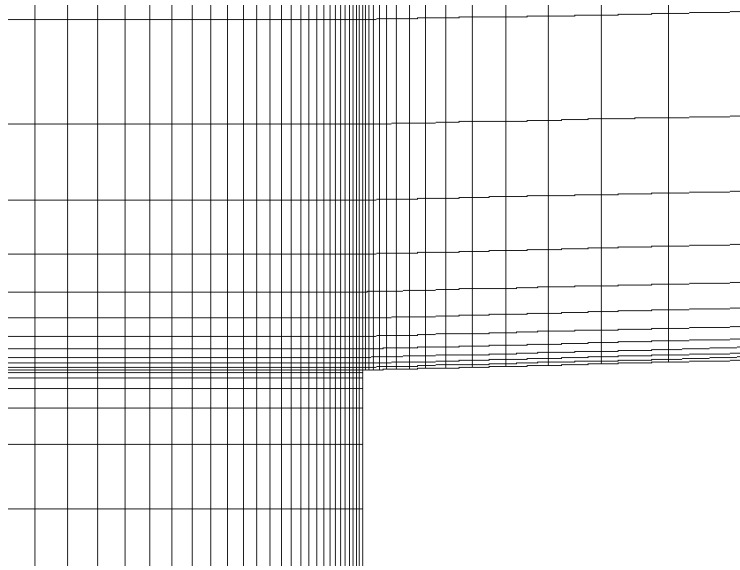Figure E.1: Cross section of the coarse LES grid.

Figure E.2: Detailed cross section of the dead zone-main channel corner for the coarse LES grid.
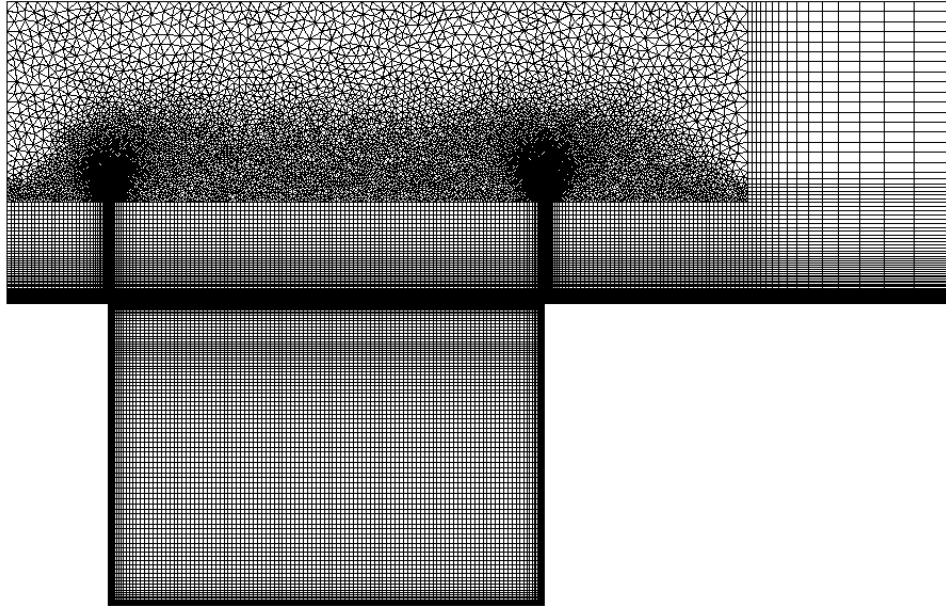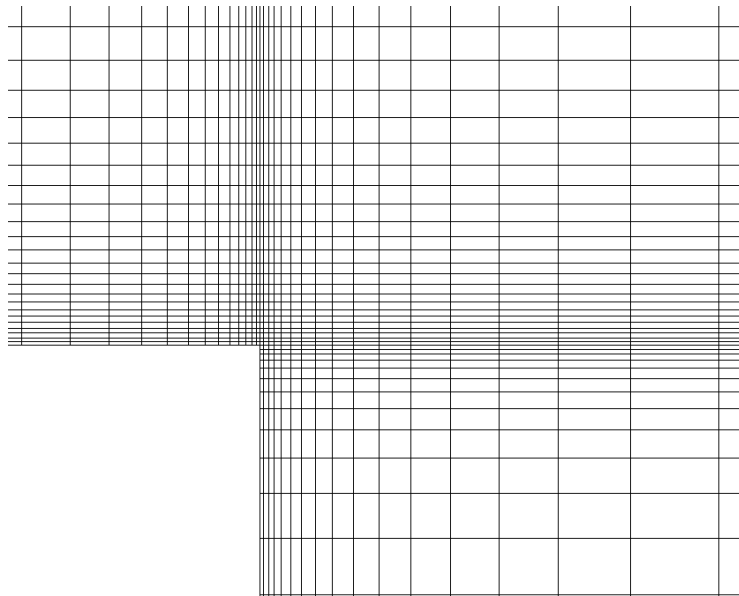
Figure E.3: Plan view of the coarse LES grid.

Figure E.4: Detailed plan view of the upstream corner of the dead zone for the coarse LES grid.
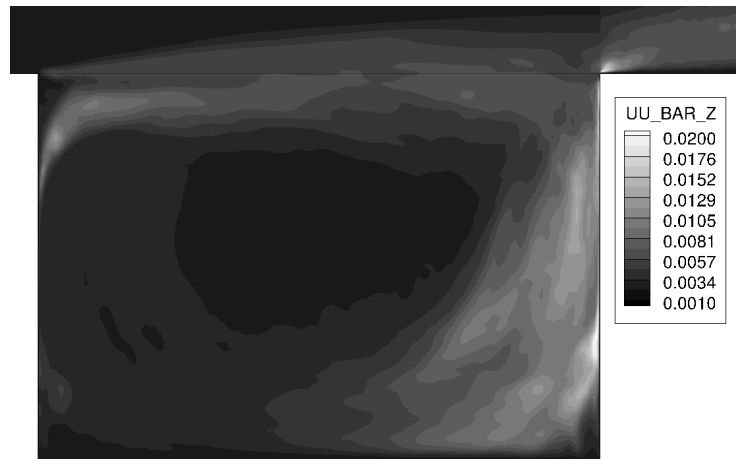
Appendix F: Additional LES Plots

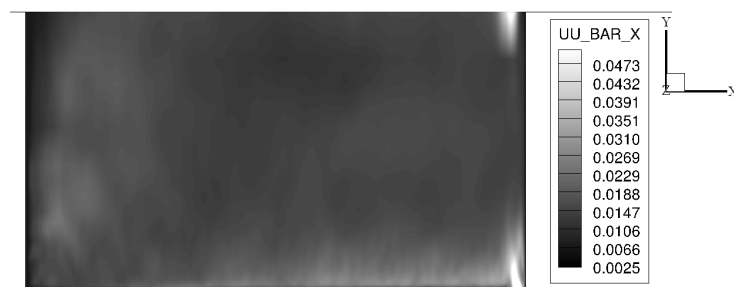Figure F.1: Plan view contours of $\frac{\overline{u_z' u_z'}}{U^2}$ at the free surface for the coarse LES grid.

Figure F.2: Plot of $\frac{\overline{u_y' u_y'}}{U^2}$ at the dead zone-main channel interface for the coarse LES grid.
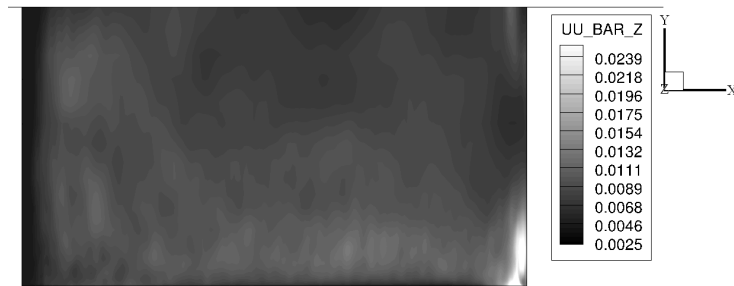
Figure F.3: Plot of $\frac{\overline{u'_z u'_z}}{U^2}$ at the dead zone-main channel interface for the coarse LES grid.